UiT

THE ARCTIC
UNIVERSITY
OF NORWAY

Faculty of Science and Technology
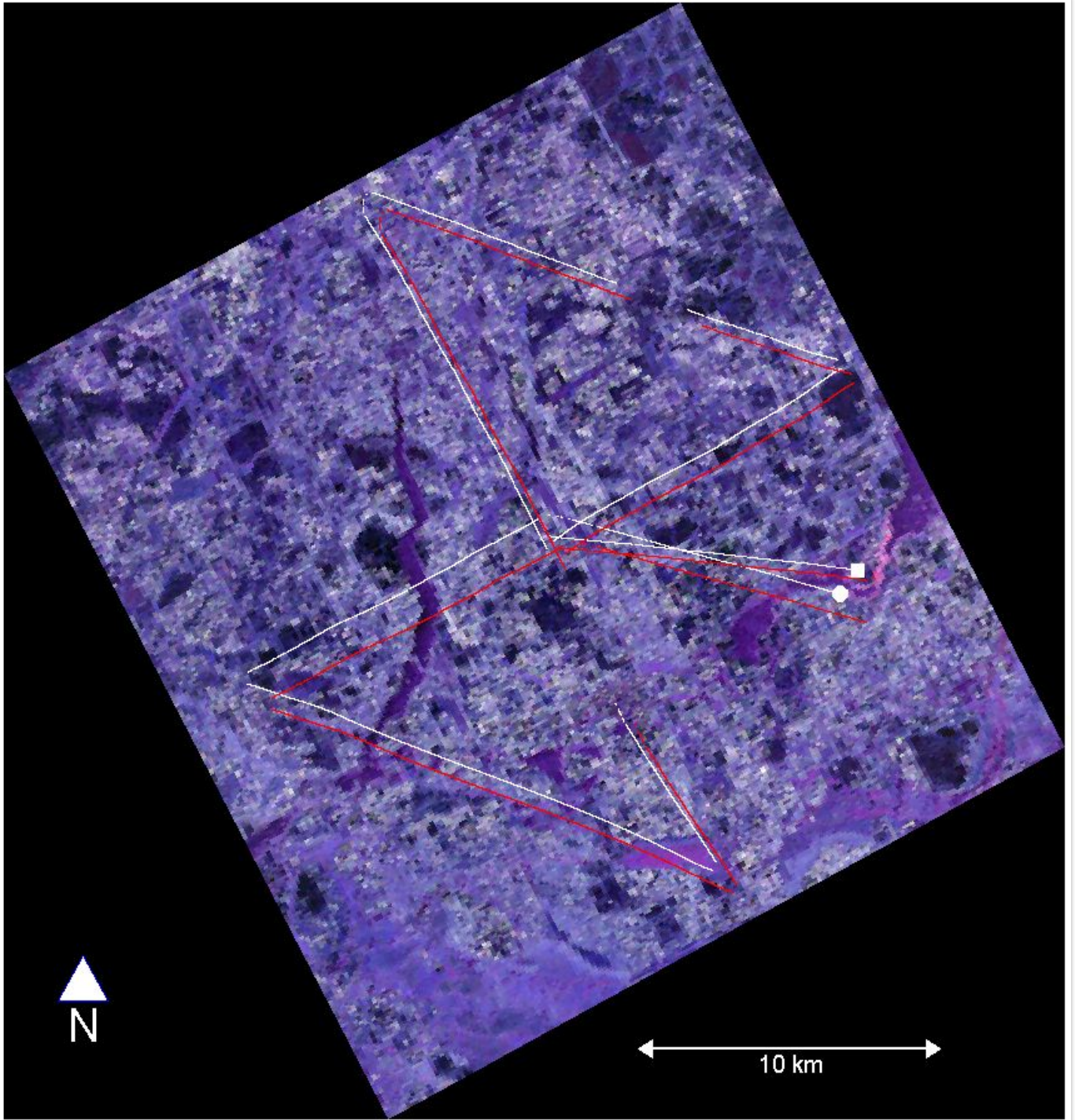
Department of Physics and Technology

Analysis and Interpretation of C-band Polarimetric SAR Signatures of Sea Ice

—

Mari-Ann Norum Moen
A dissertation for the degree of Philosophiae Doctor – November 2014

N

10 km

UNIVERSITY OF TROMSØ

«Who is the mother of the ice?
Who gives birth to the frost from the heavens?
For the water turns to ice as hard as rock,
and the surface of the waters freezes.

Can you ensure the proper sequence of the seasons,
or guide the constellation of Bear with
her satellites across the heavens? »

Job. 38, 29 - 30, 32

Abstract

At present, operational sea ice charts are manually made, a process that is inefficient and produces subjective ice charts. Hence, there is a need for automatic methods for sea ice segmentation/classification. This thesis investigates how polarimetric microwave radar signatures relate to the physical properties of sea ice, and how these signatures may contribute to the development of robust automatic segmentation/classification algorithms. Our analyses are performed on a dataset acquired during Arctic winter conditions north of Svalbard in April 2011. The dataset includes several full polarimetric C-band RADARSAT-2 SAR scenes, co-located in time and space with various in-situ data. The ice cover in the study area comprises patches of open water (leads) and first-year ice at different stages of development.

The thesis is composed of three papers. In the first paper we investigated the performance of a feature based automatic algorithm, which segments the satellite scene into a pre-defined number of classes. We performed comparisons of the automatic segmentation and two manual drawn ice charts. The succeeding analyses included labelling of the automatic segmentation in terms of ice types and interpretation of the SAR features with respect to physical sea ice properties.

The performed comparisons revealed big discrepancies between the ice charts. We demonstrated that incorporating polarimetric information in sea ice charting increased the efficiency, exactness and details in the maps. The number of classes parameter input to the segmentation algorithm was shown to be of significant importance.

The main objective of the second paper was to explore the transferability of results obtained under slightly varying environmental conditions and different viewing geometries. Three overlapping SAR scenes from consecutive days were incidence angle corrected and automatically segmented. Utilising the middle scene as reference, we considered two strategies for class labelling of the other scenes. The first is a manual labelling based on visual inspection of the scenes; the second employs various statistical distance measures to automatically assign each unlabelled class to the statistically nearest reference class. The two test scenes were also classified pixel-wise by a supervised classification based on the reference scene.

The individual automatic segmentations appeared reasonable. For the scene with the least deviating incidence angle with respect to the reference scene, all distance measure based labels agreed with the manually matched labels. The supervised pixel-wise classification also appeared reasonable. For the other scene, none of the distance measures produced results similar to the manually matched labels, and the supervised classification was very poor. The analysis showed that under stable environmental conditions and an incidence angle difference of $\sim 7°$ between the reference scene and the test scene, the results were reasonable.

In the third paper we investigated the classification potential of 44 different polarimetric features. The objective was to identify which combination of features that produces the highest classification accuracy. In addition, we intended to provide a physical interpretation of this feature combination in terms of sea ice properties. Ground-truth pixels

i

were manually selected and input to an automatic feature selection process. A non-parametric model of the class probability density function and the maximum likelihood classification were used to classify the scene. The feature subsets were evaluated based on the number of correctly classified pixels.

The best feature subset included six features. Three of them could be physically interpreted. The maximum classification accuracy arrived at approximately 70%, which reflects the complexity of the investigated scene.

The introductory part of the thesis summarises some basic theoretical background, introduces and defines important terms and concepts relevant to the research topic.

Acknowledgements

Contents

List of Tables

List of Figures

ix

Nomenclature

List of Notation

δ_{sr}	slant range resolution
c	speed of light
B	pulse bandwidth
δ_{gr}	ground range resolution
δ	incidence angle
δ_{ar}	azimuth resolution
θ_a	azimuth beamwidth
λ	radar wavelength
R	slant range, distance from antenna to target
L_a	physical antenna length
$E^{(r)}$	received electromagnetic field
$E^{(t)}$	transmitted electromagnetic field
j	imaginary unit
k	wave number
$\mathbf{S}$	scattering/sinclair matrix
$\vec{s}_C$	scattering/covariance vector
P_{tot}	total measured power
$Tr(\,)$	trace operation of matrix
$(\,)^H$	Hermitian transpose operation
$\mathbf{C}$	polarimetric covariance matrix
L	nominal number of looks
$(\,)^*$	complex conjugation
$\langle\,\rangle$	sample mean
$\mathbf{T}$	coherency matrix
$\mathbf{U}$	special unitary transformation matrix
Δh	relative height variation
ϵ^*	complex dielectric constant/electric permittivity
ϵ_0	free-space dielectric constant
ϵ'	relative dielectric constant/relative permittivity
ϵ''	dielectric loss factor

$\vec{X}$	feature vector
$P(\omega_i\|\vec{X})$	posterior probability
$p(\vec{X}\|\omega_i)$	class-conditional probability density function
$P(\omega_i)$	a priori probability of class ω_i
I_{HH}	backscattered HH intensity
I_{HV}	backscattered HV intensity
I_{VV}	backscattered VV intensity
GB	geometric brightness
$SPAN\{C\}$	span of **C**-matrix
$R_{VV/HH}$	co-polarization ratio
$R_{HV/B}$	cross-polarization ratio
ρ	co-polarization correlation coefficient
$\vec{u}_i$	i^{th} eigenvector of the coherency matrix
λ_i	i^{th} eigenvalue of the covariance/coherency matrix
PH	Pedestal Height
PF	Polarization Fraction
PA	Polarization Asymmetry
H	Entropy (H/A/α)
P_j	pseudo-probability of λ_j
A	Anisotropy, (H/A/α)
$\overline{\alpha}$	mean α-angle (H/A/α)
$\vec{u}_i^{TSVM}$	normalised eigenvector of the coherency matrix (TSVM)
α_s	magnitude of the maximum polarisation response (TSVM)
τ_m	helicity of the maximum polarisation response (TSVM)
ψ_s	orientation angle of the maximum polarisation response (TSVM)
$\Phi_{\alpha s}$	phase of the maximum polarisation response (TSVM)
Φ_s	absolute phase of the target (TSVM)
$\mathbf{C}^{\mathrm{rem}}$	remainder matrix component of the covariance matrix (NNED)
c^{vol}	volume component scaling factor (NNED)
$\mathbf{C}^{\mathrm{vol}}$	volume matrix component of the covariance matrix (NNED)
$\mathbf{C}^{\mathrm{sgl}}$	single-bounce matrix component of the covariance matrix (NNED)
λ^{sgl}	single-bounce scaling factor (NNED)
$\mathbf{C}^{\mathrm{dbl}}$	double-bounce matrix component of the covariance matrix (NNED)
λ^{dbl}	double-bounce scaling factor (NNED)
λ^{rem}	remainders scaling factor (NNED)
I^{vol}	volume intensity (NNED)
I^{sgl}	single-bounce intensity(NNED)
I^{dbl}	double-bounce intensity(NNED)
RK	relative kurtosis
Z_i	total snow plus ice thickness
h_w	distance between the EM-bird and sea water surface
h_i	distance from EM-bird to the snow/ice surface

List of Acronyms

AVHRR	Advanced Very High Resolution Radiometer
CCRS	Canada Centre for Remote Sensing
CIA	Centre Incidence Angle
CIS	Canadian Ice Service
CP	Compact Polarimetry
EM	Electromagnetic
GAR	Ground Azimuth Resolution
GB	Geometric Brightness
GPS	Global Positioning System
GRR	Ground Range Resolution
IEEE	Institute of Electrical and Electronic Engineers
IPCC	Intergovernmental Panel on Climate Change
ISVP	Iridium Surface Velocity Profiler
KDE	Kernel Density Estimation
KSAT	Kongsberg Satellite Services
MAGIC	Map Guided Ice Classification
ML	Maximum likelihood
MODIS	Moderate Resolution Imaging Spectroradiometer
MRF	Markov Random Field
NASA	National Aeronautics and Space Administration
NIC	U.S. National Ice Center
NNED	Non-Negative Eigenvalue Decomposition
NSC	Norwegian Space Centre
NWP	Numerical Weather Prediction
PA	Polarization Assymmetry
PALSAR	Phased Array type L-band Synthetic Aperture Radar
pdf	probability density function
PF	Polarization Fraction
PH	Pedestal Height
quad-pol	quadrature polarization
QUIKSCAT	Quick Scatterometer
RADAR	Radio Detection And Ranging
RADARSAT	RADAR Satellite
RCM	Radarsat Constellation Mission
RGB	Red-Green-Blue
RK	Relative Kurtosis
SAR	Syntethic Aperture Radar
SLC	Single-Look Complex

SSM/I   Spesial Sensor Microwave/Imager
SoD   Stage of Development
TSVM   Target Scattering Vector Model
UNFCCC   United Nations Framework Convention on Climate Change
UTC   Universal Time Coordinated
WMO   Word Meteorological Organization

Chapter 1

Introduction

1.1 Motivation

In the latest years sea ice research reports have caused media headlines every year when the sea ice extent has reached a new minimum. The latest report from the Intergovernmental Panel on Climate Change (IPCC) states that the annual Arctic sea ice extent decreased by 3.5% - 4.1% per decade between 1979 and 2012 [Stocker et al., 2013]. It is also reported that the Arctic sea ice is getting thinner [Stocker et al., 2013, Maslanik et al., 2011, Kwok et al., 2009] and younger, i.e., the fraction of perennial and multiyear ice have decreased in the same period. Fig. 1.1 illustrates the minimum sea ice extent in 2007 and 2012 compared to the 1979-2000 average extent.

The arctic ice is declining, but why should we be concerned?
In order to understand the concern, we need to place the (Arctic) sea ice in perspective. The Arctic region is located on "the top of the world" and is a "giant jigsaw puzzle" of sea ice surrounded by land. Eight countries: Canada, Russia, the United States (Alaska), Denmark (Greenland), Norway and Iceland border on the Arctic basin.
From an economical point-of-view the retreating sea ice exposes new areas to be explored and possibly exploited. Previously ice-covered natural resources, e.g., oil and gas, are now accessible for longer periods as the seas start to freeze several weeks later than before. Fleets of ships and drilling platforms are poised to navigate in these newly opened waters [Eicken, 2013]. Navigating ships in these waters is potentially dangerous if not properly experienced, equipped and prepared.
From an environmental perspective the interest in sea ice relates to its sensitivity to changes in the global climate system. The Arctic ice is global warming's "canary in the coal mine". The condition of the ice is a climate state indicator and a harbinger of consequences to come. It controls heat, moisture and chemical fluxes between the ocean and the atmosphere, modifies the surface albedo and reallocates the salt and freshwater content in the sea. The World Meteorological (WMO) and the United Nations Framework Convention on Climate Change (UNFCCC) have both acknowledged sea ice, char-

acterised by its extent, type, concentration, thickness, motion, melt stage, surface characteristics and seasonality of coverage, as an Essential Climate Variable [Falkingham, 2014]. Changes in the climate and the extent and distribution of sea ice influence the Arctic life in general. Poor ice conditions make hunting a serious challenge for both humans and polar bears. The ice affects the marine ecosystem by controlling the heat and light entering the ocean [Falkingham, 2014].

The work we present in this thesis focuses on methods to aid and improve operational ice charting. Operational ice charts are currently produced manually by numerous national ice services. It is a time-consuming process and the resulting charts are subjective and depend heavily on the analysts' experience [Falkingham, 2014, Moen et al., 2013a, National Ice Center, 2006]. Hence, it is of great interest to develop methods, which can make ice charting more efficient and less analyst dependent by automating the whole or parts of the process. Currently, no automatic procedure has been able to meet the strong requirements of effectively producing robust and precise operational ice charts. The segmentation and classification challenges are related to the large variation in backscatter due to environmental factors and sensor artifacts. Variations in location, season and incidence angle influence the backscatter such that the same ice type can have distinctly different appearances, and different ice types can have similar appearances [Clausi et al., 2010].
The ice charts offer important information to policy makers, regulators, climate scientists, hydrologists, numerical weather prediction (NWP) organisations, emergency incident responders, fishermen, and ship and offshore platform operators. However, the charts' main purposes are to improve the safety of marine navigation and offshore operations, minimise damage on ships and offshore installations, and aid ecosystem management [Falkingham, 2014].

Collecting data from the Arctic sea ice is challenging. It is remote, harsh, mostly cloud-covered and blanketed in darkness for several months through the year. At the North Pole the polar night lasts from late September to mid-March. The area close to the ice edge is covered with clouds or fog about 70% of the time [Bertoia et al., 2004]. These difficulties are dealt with by utilising the active microwave remote sensing's advantage of making measurements independent of sunlight and atmospheric effects such as clouds, smoke and dust [Chuvieco and Huete, 2010].
Nevertheless, remote sensing of sea ice is not trivial. Sea ice is the most complex earth terrain [Onstott and Shuchman, 2004] and lack of in situ data for validation testing is a recurring issue. An important pre-requisite to the interpretation of satellite-derived signatures of sea ice is to understand the interaction between the backscattered electromagnetic (EM) signal measured by a satellite sensor and the snow, ice and ocean [Massom and Lubin, 2006a]. The overall objective of the work presented in this thesis is to relate parameters derived from multi-channel SAR scenes to real physical ice types in order to produce reliable ice charts under changing environmental conditions and varying viewing geometry. It is our desire that this work will contribute to the development

of robust, high-resolution sea ice classification maps from SAR imagery.

Although scenes of four polarisation channels (quad-pol) are significantly smaller than dual and single polarisation (dual-pol, single-pol) scenes in terms of spatial coverage, they are more detailed and contain more geophysical information. Hence, they are considered of invaluable importance with respect to understanding the nature of the microwaves' interaction with the ice surface and hence the relationship between the sea ice signature in a SAR image and physical sea ice properties.

Space-borne microwave sensors also have benefits such as frequent coverage (high temporal resolution), high spatial resolution and vast spatial coverage. The work presented in this thesis uses the Canadian RADARSAT-2 synthetic aperture radar (SAR) sensor. This sensor can produce images with resolution up to 1 m $\times$ 3 m (spotlight mode) and swath widths up to 500 km (ScanSAR wide mode). The revisit period of a satellite depends on different parameters, e.g., incidence angle and geographical location. The RADARSAT-2 satellite is able to provide an image of the exact same geographical area with the exact same beam mode and position in 24 days [Morena et al., 2004]. However, if the exact beam requirements are not crucial a much shorter revisiting time is possible. The above-mentioned specifications justify why SAR is the sensor of choice in operational ice charting.
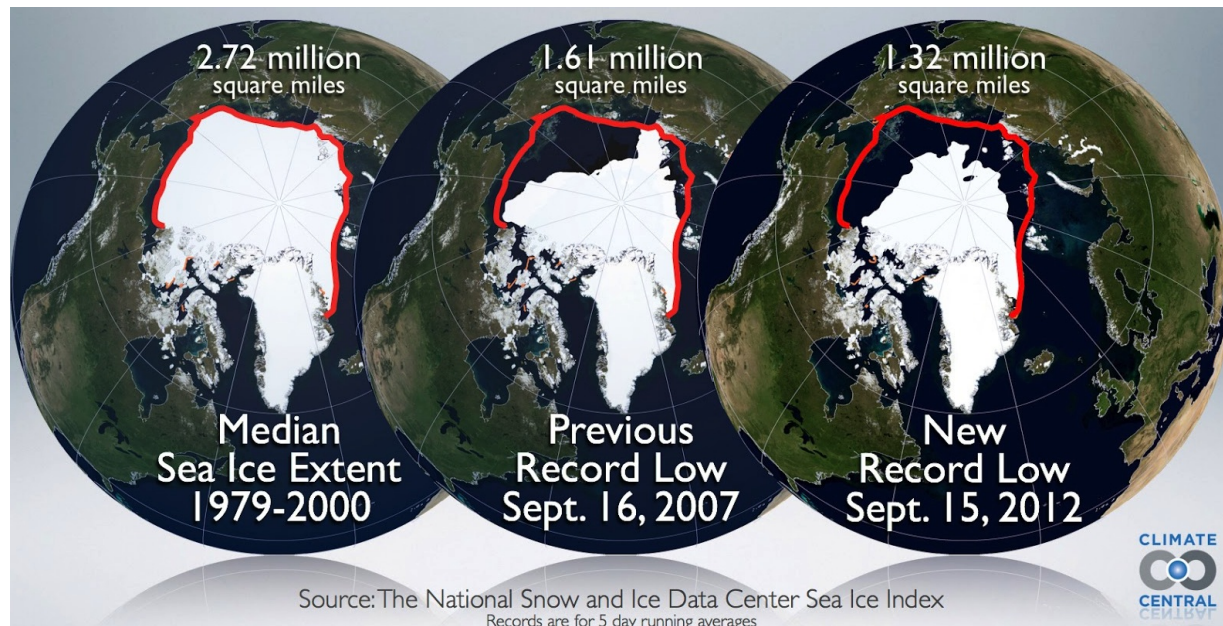
Figure 1.1: Arctic sea ice extent. Left globe: Average 1979-2000 sea ice extent (red line), Middle globe: 2007 minimum ice extent compared to 1979-2000 average extent (red line), Right globe: 2012 overall recorded minimum compared to 1979-2000 average extent. Image Courtesy of Climate Central, www.climatecentral.org.

The research contribution of the thesis is composed of three papers. All three papers are based on SAR scenes obtained under winter conditions, i.e., no melting of the ice, in April 2011. The scenes are located north of Svalbard. A more thorough description of the dataset is provided in chapter 5. The uniqueness of the dataset is related to the short time span between the image acquisition and the obtaining of in-situ measurements, i.e., drift measurements, thickness measurements and optical photos retrieved during helicopter flights.

In the following the terms *segmentation* and *classification* have slightly different meanings. *Segmentation* is the process of dividing an image into different non-contiguous areas of similar statistical properties. The result of such a process is referred to as *a segmentation*. We further define *classification* as the task where each pixel or unlabelled area is assigned to a labelled class, i.e., an ice type.
The main objectives of the three papers can be summarised as follows:

- compare manually and automatically generated maps and examine how well they correspond (Paper 1).

- investigate polarimetric SAR features and their ability to segment and classify different ice types (Paper 1 and Paper 3).

- investigate the physical interpretation of various polarimetric features with respect to ice types (Paper 1 and Paper 3).

- explore the possibility of transferring information obtained from one scene to two other scenes obtained from consecutive days (Paper 2).

- investigate how a carefully selected subset of polarimetric features influences the classification accuracy (Paper 3).

1.2 Chapter Review

Chapter 2 provides basic background information about SAR. The inherent noise-like phenomenon in all coherent imaging systems known as speckle is briefly explained. Then we describe the viewing geometry of a SAR and how it relates to the obtained image resolution. The last two sections of this chapter look into the concept of polarimetry and polarimetric decompositions.

Chapter 3 starts by providing background information about microwave backscatter properties related to sea ice. Four physical properties, namely, surface roughness, viewing and surface geometry, the complex dielectric constant, and the existence of dielectric discontinuities are outlined. These are followed by a description of the different sea ice types or stages of development (SoD) as defined by the WMO. The next section briefly

explains how operational sea ice charts are currently made. Finally, we provide a description of categories we have used to categorise various automatic sea ice classification/segmentation methods.

Chapter 4 is divided in four main sections. Each section describes a category of features and provide a brief description of features utilised in the presented work that belongs to the category. A physical interpretation of each feature is provided if such exists.

Chapter 5 - 7 contain Papers 1 - 3. An extended abstract of each paper is given in the next section 1.3.

Chapter 8 summarises the conclusions of the presented work, provides thoughts concerning challenges to overcome and ideas for future studies.

1.3   Publication Review

Paper 1

M.-A. Moen, A. P. Doulgeris, S. N. Anfinsen, A. H. H. Renner, N. Hughes, S. Gerland, and T. Eltoft, **Comparison of feature based segmentation of full polarised SAR satellite sea ice images with manually drawn ice charts**, The Cryosphere, vol. 7, pp 1693 - 1705, November 2013.

This paper investigates sea ice type retrieval from a quad-polarimetric RADARSAT-2 scene acquired north of Svalbard in April 2011. The details of quad-pol images are of significant importance in order to understand the underlying physics of radar backscatter from sea ice. The satellite scene is automatically segmented into a predefined number of classes utilising statistical and polarimetric properties of the backscattered signal. The automatic unsupervised mixture-of-Gaussian segmentation algorithm utilises six real-valued features extracted from the polarimetric covariance matrix. Five features are commonly used polarimetric parameters, e.g., cross-pol ratio and brightness. The sixth feature, the relative kurtosis, has not previously been used for sea ice segmentation or classification. The consistency between ice charts is investigated by comparing the automatic segmentation with two manually drawn SoD ice charts independently produced by two ice analysts. The differences between the two hand-drawn charts are also evaluated. In the subsequent analysis, ice experts label the segments of the automatic segmentation aided by available in-situ measurements (snow plus ice thickness measurements and optical images obtained during a helicopter flight). The six features used in the automatic segmentation are interpreted in terms of physical sea ice properties.

Our results reveal some degree of inconsistency in all three ice chart comparisons. That is, the number of classes disagrees in all ice charts. This confirms the idea of manual

ice charting being analyst dependent. Manually generated ice charts are commonly used for validation of automatic classification methods. This study demonstrates that manual SoD ice charts must be applied with care for validation purposes. We suggest that by utilising polarimetric SAR features in sea ice segmentation the ice charts become less subjective. The features may also aid the labelling of the automatically segmented scene. The "new" relative kurtosis parameter shows good classification power in terms of separating deformed and smooth ice and makes a valuable contribution to the segmentation.

The utilised automatic algorithm divides the SAR scene into five distinct unlabelled classes. The optical images, acquired from a helicopter flight, made it possible for the ice experts to label three ice classes. A physical interpretation of the polarimetric features supported the labelling of the remaining segments. We suggest that automatic labelling can be based on statistical distribution models of polarimetric parameters that can be physically interpreted in terms of ice type.

The number of classes is a key input parameter, which constrains the segmentation algorithm. A too low number of classes will result in mixed classes. Contrarily, a too high number of classes forces the algorithm to split real classes and hence present an end result with "artificial" classes. Choosing the "right" number of classes is a complicated problem; nevertheless, future work should aim at robust and automatic estimation of the number of classes.

The season, in particular melting conditions during late spring, summer and early fall, will affect the microwave backscatter of sea ice [Kwok et al., 1992]. Thus, the polarimetric properties and their numerical values for a given ice class may not be directly transferable from one season, or even one day, to another. However, given that the environmental conditions are reasonable stable, it may be possible to incorporate a priori information such as ice charts from previous days into the classifier. The transferability of information from one scene to another is investigated in Paper 2 [Ch. 7].

Due to the limited swath width, full polarimetric SAR data are less suited for operational ice charting than dual-pol. However, future compact polarimetry sensors like PALSAR-2 (Phased Array type L-band syntethic aperture radar) and the Radarsat Constellation Mission (RCM) provide wide coverage scenes. The method we present may be extended to compact polarimetry. This will be an important topic for future work.

Six features are utilised for automatic classification in this paper. In Paper 3 [Ch. 8] we explore the classification potential of these six together with 38 additional features.

Paper 2

M.-A. Moen, S. N. Anfinsen, A. P. Doulgeris, A. H. H. Renner, S. Gerland, **An inter-comparison of techniques to classify polarimetric SAR images of sea ice**, in review Annals of Glaciology.

In this paper we investigate the transferability of polarimetric features between three RADARSAT-2 scenes obtained under slightly changing environmental conditions and acquired at different incidence angles. The full polarimetric SAR scenes have good geographical overlap and are acquired under freezing conditions at consecutive days north of Svalbard in April 2011.

The backscattered signal is incidence angle dependent. Thus, prior to further analysis the first and the last scene are incidence angle corrected using the middle scene as reference.

All three scenes are segmented using an unsupervised mixture-of-Gaussian segmentation algorithm and subsequently smoothed in order to decrease the effects of speckle and ease the interpretation. The segmentation method utilises six features extracted from the polarimetric data.

The middle scene is the same as the one investigated in Paper 1, hence prior knowledge, e.g., classification results, from that survey is employed in this paper.

Using the middle scene as reference we consider two strategies for labelling the two test scenes. The first method implies manual matching based on visual inspection of the segmentations. The second method utilises five statistical distance measures (the Mahalanobis distance, the Multivariate Gaussian Bhattasarrya distance, the symmetric Multivariate Gaussian Kullback-Leibler distance and the Complex-Wishart Kullback-Leibler distance) to automatically assign each unlabelled class to the statistically nearest reference class. We also performed a pixel-wise supervised classification assigning each pixel to the statistical nearest class in the reference data.

Our results show that the segmentation result for each scene individually looks reasonable. However, when we try to use the reference scene to label the unlabelled classes in the test scenes, the results disagree. The classification from the manually matched labels and the automatic labelling are identical for the last scene. For the first scene, none of the distance measures make the automatic labelling correspond perfectly to the manually matched labelling. When we consider both test scenes, the labelling utilising the Mahalanobis distance performs best.

The pixel-wise supervised classification appears reasonable for the last scene, but are very poor for the first scene. We have indications that this may be related to the different incidence angles. The first scene is the scene that differs the most from the reference scene with respect to incidence angle. The two test scenes were incidence angle corrected to a first order approximation, but this does obviously not fully account for the differences between the scenes. However, we conclude that the advantages of the

7

correction are greater than the disadvantages. A proper incidence angle correction is crucial for comparison of scenes obtained at different incidence angles and is a highly relevant topic for future work.

The presented work has potential for operational use. It demonstrates reasonable results for similar incidence angles and freezing conditions.

The presented segmentation algorithm utilises six features extracted from the polarimetric SAR scene. In Paper 3 [Ch. 8] we investigate the classification potential of 44 polarimetric features, including the six used in the current paper.

Paper 3

M.-A. Moen, S. N. Anfinsen, A. P. Doulgeris, T. Eltoft, **Feature selection for sea ice classification of polarimetric SAR scenes**, submitted to Journal of Sensors in Oct. 2013. The main objective of this paper is to investigate the classification potential of an initial set of 44 polarimetric parameters. We aim to answer the two following key questions, (i) which feature subset is the optimal with respect to classification accuracy, and (ii) how can the selected features be interpreted in terms of sea ice properties and ice type.

All 44 parameters are extracted from the C-matrix, whereof 34 features are extracted using the Polarimetric SAR Data Processing and Educational toolbox (PolSARpro) v.5 software. 25 of these 34 parameters are derived from three polarimetric decompositions, i.e., the $H/A/\alpha$ decomposition, the non-negative eigenvalue decomposition (NNED) and the target scattering vector model (TSVM). We have also included the six features utilised for sea ice segmentation and classification in our previous studies (Paper 1 and Paper 2).

Ice type training samples from five distinct ice types are manually chosen based on visual inspection of in-situ data and an RGB representation of the satellite scene. The classification performance of each subset is explored by using the Bayesian based maximum likelihood (ML) classifier. Each of the training samples is classified to the most probable class using the class-conditional probability density function (pdf). Since we do not want to restrict the analysis to a certain model we estimate the class-conditional pdf using multivariate kernel density estimation (KDE). The KDE is a non-parametric method that estimates a free-form distribution from a given training set as a linear combination of kernels centred at the training points. In the current study we have used Gaussian kernels with standard deviation equal to one.

An optimal search for the best feature subset requires an exhaustive testing of all possible feature subsets. Given 44 features this is not feasible. Hence, we apply the suboptimal searching technique known as the sequential forward feature selection (SFFS)

method. The classification accuracy is calculated from a performance criterion, the Producer's Accuracy, that automatically account for correlated features. That is, if a feature to be added is highly correlated to any of those in the existing subset it will most likely not significantly improve the classification accuracy, and hence be added at one of the latest stages.

We found that the best feature subset comprises six features, whereof half of them can be physically interpreted. The maximum achieved classification accuracy is $\sim 70\%$, which reflects the complexity of our scene.

Our investigation demonstrates that the sea ice classification can be improved by systematically selecting the best feature subset. However, the best combination of features will vary with season, environmental conditions, incidence angle and the optimality criterion employed. The proposed feature selection method will be appropriate for a semi-automatic classification algorithm. An experienced sea ice analyst can carefully decide the number of classes and select the training samples for each class. A pixel-wise automatic classification can then be produced from the chosen subset. This method is generic and also suitable for dual- and single-pol satellite scenes.

1.4 Other Scientific Contributions

1. Moen M.-A., Anfinsen S.N, Doulgeris A.P., Renner A.H.H., Gerland S., *Assessing the robustness of sea ice classifications from polarimetric radar images*, IGS symposium on sea ice in a changing environment, Hobart, Australia, March, 2014, (oral presentation).

2. Moen, M.-A., Ferro-Famil L., Doulgeris A. P., Anfinsen S. N., Gerland S. and Eltoft T., *Polarimetric decomposition analysis of sea ice data*, Proc. POLinSAR 2013, Frascati, Italy, January/February, 2013.

3. Moen M.-A., Doulgeris A.P., Anfinsen S.N., Hughes N., Renner A.H.H., Gerland S., Robertsen T., Lund V., Eltoft T., *Comparison of feature based segmentation of SAR satellite sea ice images with manually drawn ice carhts*, Proc. Earth Observation and Cryosphere Science, Frascati, Italy, November, 2012.

4. Moen M.-A., Anfinsen S.N., Doulgeris A.P., Gerland S., Eltoft T., *Physical significance of radar texture in sea ice studies*, POLinSAR 2011, Frascati, Italia, January, 2011, (oral presentation).

In addition to the listed contributions, the Ph.D candidate has also been involved in other co-authored work at the university of Tromsø - the Arctic university of Norway, the Norwegian Polar Institute, and the Ice Service at the Norwegian Meteorological Institute.

Chapter 2

Space-borne Imaging Radar - Synthetic Aperture Radar (SAR)

2.1 RADAR principle

In general, all *radar* (RAdio Detection and Ranging) sensors are based on the principle of echolocation. A signal is transmitted and the returned echoes are measured. When the speed of the signal is known, we can estimate the distance to a target based on the travelling-time (back and forth) of the signal. Bats are well-known for their technique of mapping their surroundings - a natural active remote sensing system. A bat senses the world in terms of surface roughness, acoustic reflectivity and relative motion, not in terms of colour. This is comparable to the way a radar system pictures the surroundings [Woodhouse, 2006].

After the first successful launch of a SAR, Seasat in 1978, imaging radars have emerged as an immensely powerful and indispensable Earth remote sensing instrument [Lee and Pottier, 2009, Massom and Lubin, 2006b]. They are particularly important in regions where the hostile climate, the remoteness, and the seasonal lack of daylight limit the availability of in situ data, such as the polar areas [Clausi and Deng, 2003]. The SAR imaging system is operating in the microwave region (see Table 2.1) of the electromagnetic (EM) spectrum. This, in combination with being active, i.e., generating its own illumination, makes the SAR operable regardless of weather and daylight.

2.1.1 Speckle

Speckle is inherent in all coherent imaging systems and causes a spurious pixel variation in intensity and appears in the images as "salt and pepper" noise. Strictly speaking, speckle is not noise because it is a deterministic and repeatable phenomenon [Wood-

---

[1]Frequencies from 216 - 450 MHz are sometimes referred to as P-band.

[2]The official ITU designation for the ultra high frequency band extends to 3000 MHz. In radar practice the upper limit is set to 1000 MHz as L- and S-band are used to describe the higher UHF region.

Radar letter designation	Frequency	Wavelength
VHF[1]	30 - 300 MHz	1 - 10 m
UHF[1,2]	300 - 1000 MHz	30 - 100 cm
L-band	1 - 2 GHz	15 - 30 cm
S-band	2 - 4 GHz	7.5 - 15.0 cm
C-band	4 - 8 GHz	3.75 - 7.5 cm
X-band	8 - 12 GHz	2.5 - 3.75 cm
Ku-band	12 - 18 GHz	1.67 - 2.5 cm
K-band	18 - 27 GHz	1.11 - 1.67 cm
Ka-band	27 - 40 GHz	0.75 - 1.11 cm

Table 2.1: Frequency and wavelength of different microwave bands used by active remote sensing sensors. After [IEEE standards, 2003].

house, 2006, Oliver and Quegan, 2004]. It originates from the constructive/destructive interference among the echoes of the individual scatterers within one resolution cell. The speckle phenomenon degrades the image and complicates image interpretation. Several methods for speckle reduction exist [Lee and Pottier, 2009]. The multilooking process, described in section 2.3.3, averages over a set of neighbouring pixels and consequently smoothes the speckly appearance. It can be seen as a naïve speckle filter.

2.2 SAR Geometry and Resolution

Figure 2.1 illustrates a simplified geometry of a satellite-borne side-looking SAR system. The satellite moves in the azimuth/along-track direction and illuminates an area commonly known as the *beam footprint*.

The image resolution is defined as the separation between the two closest objects that still can be distinguished in the final image [van Zyl and Kim, 2011]. The received echoes from two point targets must have a time difference less than, or equal to, the length τ of the radar pulse to be recognised as two distinct targets. The *slant range* resolution of a radar is given by [van Zyl and Kim, 2011]:

$$\delta_{sr} = \frac{c}{2B} \, , \tag{2.1}$$

where c is the speed of light and B is the pulse bandwidth. The factor 2 appears because of the two-way travel time of the pulse. Typical bandwidths of space-borne SAR pulses range between 10 and 40 MHz, giving a slant range resolution of 15 to 3.75 meters [McCandless Jr. and Jackson, 2004]. The ground resolution, δ_{gr}, is the change in ground range associated with a slant range of δ_{sr} and incidence angle θ. Straightforward trigonometry leads to the following expression for the ground resolution [Woodhouse,
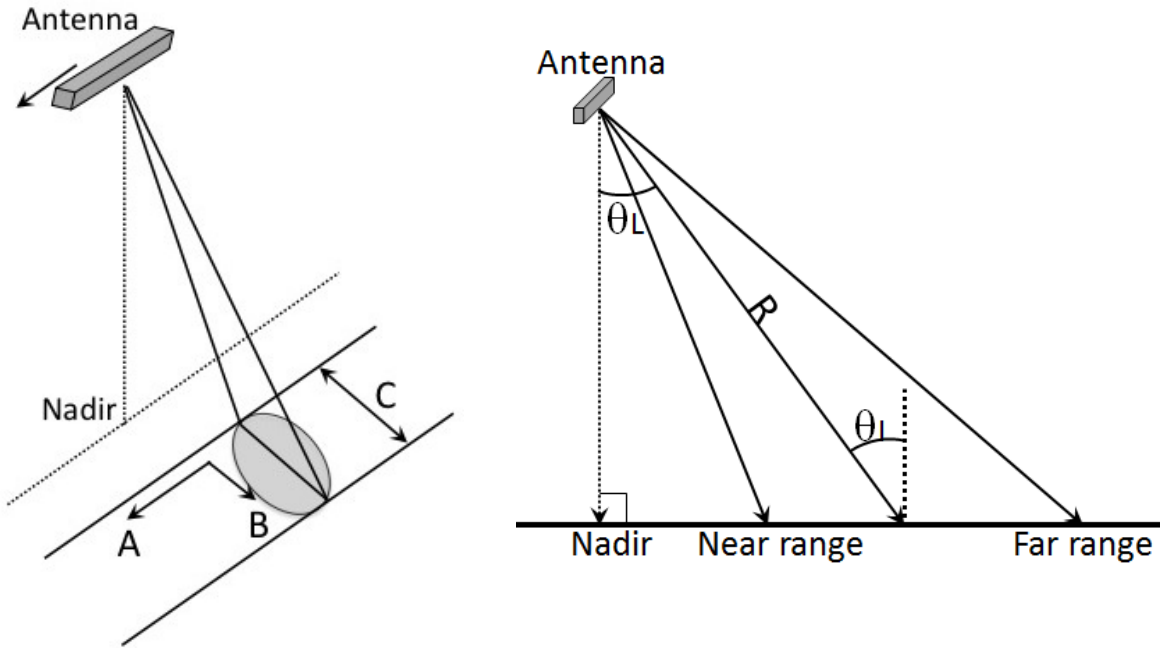
(a) Nadir is the point on the ground directly beneath the platform, A and B represents the azimuth/along-track and the range/across-track dimensions, respectively. C is the swath width.

(b) θ_L is the radar look angle and θ_I is the radar centre incidence angle (CIA). In a flat earth geometry with no terrain $\theta_L = \theta_I$. R is the shortest distance between the radar and a point on the ground, known as slant range.

Figure 2.1: Simplified SAR geometry.

2006]:

$$\delta_{gr} = \frac{\delta_{sr}}{\sin \theta} \tag{2.2}$$

From the above equation it is apparent that the ground range resolution changes non-linearly across the swath and increases as the incidence angle increases. That is, the near range of an image swath has poorer resolution than the far range of the swath.

In conventional radar systems the azimuth resolution (δ_a) is determined by the azimuth beamwidth (θ_a), which depends on the radar wavelength (λ) and the physical size of the antenna (L_a). The azimuth resolution is

$$\delta_a r \approx R\theta_a \approx \frac{R\lambda}{L_a}, \tag{2.3}$$

where R is the distance from the antenna.

It is apparent from eq. (2.3) that the azimuth resolution can be improved by increasing the antenna length. However, it is inconvenient with large antennas, especially in

space. Fig. 2.2 illustrates how a uniform, fine azimuth resolution across the entire imaging swath can be achieved by simulating a very long antenna, a technique known as synthetic aperture radar (SAR).
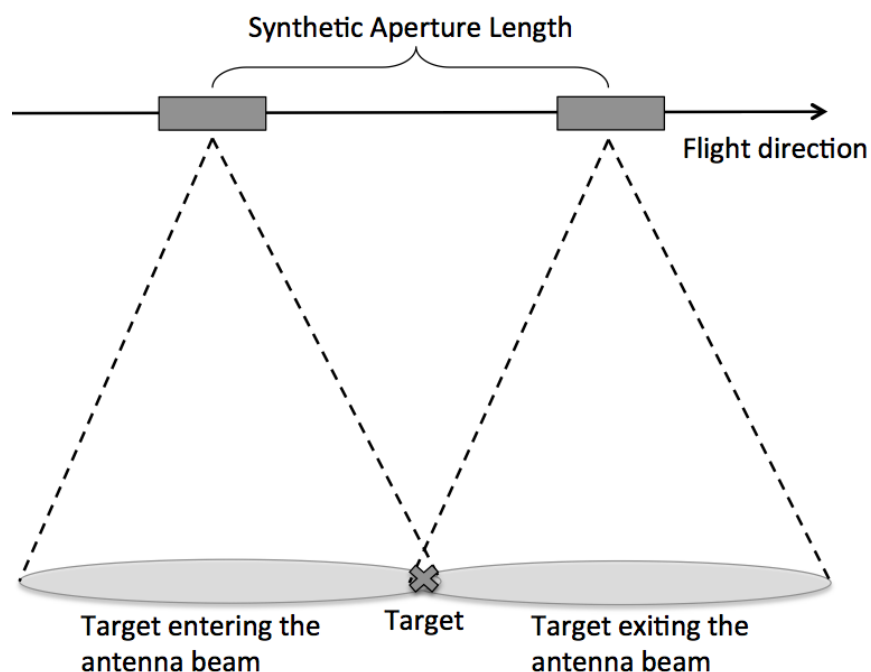
Figure 2.2: The SAR principle. The synthetic aperture length is the length of the sensor path during the time a target stays within the radar beam.

Geometrical distortions related to steep hillsides inside the scene may occur. This is not an issue in the presented work, as we are imaging "flat" areas, i.e., no land areas. If satellite scenes with both land and ice were to be classified using methods presented in this thesis we suggest that land areas are masked out prior to further processing.

2.3 Polarimetry

Electromagnetic (EM) waves are transverse, that is, the oscillations are perpendicular to the direction of travel of the wave, similar to the "up" and "down" oscillations on a rope [Griffiths and College, 1999]. The *polarisation* of an EM wave is described by the shape the electric field vector would draw in time at a fixed point in space. If we use the rope analogy, shaking it up and down represent the *vertical* polarisation. Whereas shaking the rope left and right corresponds to the *horizontal* polarisation. Both examples are illustrated in Fig. 2.3. When the tip of the electric field traces out a straight line in xy-plane, the wave is said to have a *linear* polarisation. The oscillation may also occur

in any other direction of the xy-plane. If a circle is traced out, the wave is *circularly polarised*. [Woodhouse, 2006].
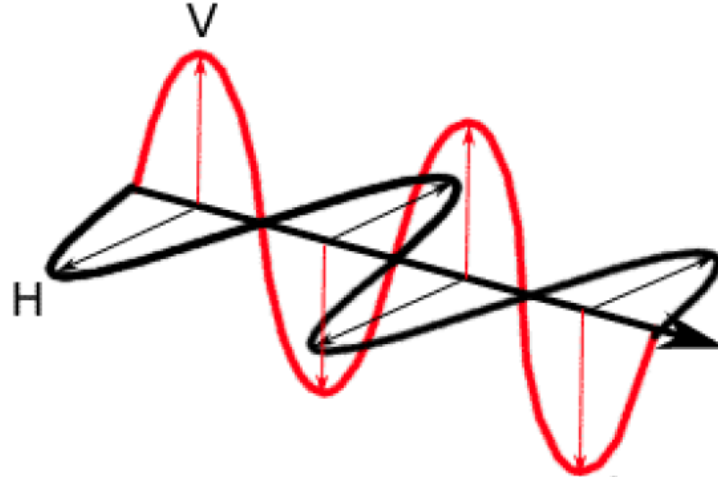
Figure 2.3: Electromagnetic waves with a horizontal (H) polarisation in black, and a vertical (V) polarisation in red. Image courtesy of [Canadian Centre for Remote Sensing, 2007].

A full polarimetric SAR instrument transmits orthogonally polarised microwave pulses and measures the orthogonally components of the returned electromagnetic (EM) waves. The backscattered wave depends on the properties of the illuminated scatterers, e.g., dielectric properties and geometrical structure, and sensor parameters, e.g., incidence angle, frequency, polarisation and noise [Elachi and van Zyl, 2006, Chuvieco and Huete, 2010]. Thus, the impact of the target can be considered as a mathematical operator that takes one two-dimensional complex vector (the transmitted EM wave) and transforms it into another two-dimensional complex vector (the received/scattered EM wave). This transformation can be expressed as

$$
\begin{bmatrix} E_x^{(r)} \\ E_y^{(r)} \end{bmatrix} = \frac{e^{-jkR}}{R} \begin{bmatrix} S_{xx} & S_{xy} \\ S_{yx} & S_{yy} \end{bmatrix} \begin{bmatrix} E_x^{(t)} \\ E_y^{(t)} \end{bmatrix}
\tag{2.4}
$$

where $j = \sqrt{-1}$ is the imaginary unit, k is the wave number and R is the distance between the target and the radar. The superscripts of the EM field components indicate whether it is the received (r) or transmitted (t) field component. The subscripts of the EM field refer to the associated polarisation of the wave. In general, the polarisations x and y could be any orthogonal polarisations, although, it has been assumed that the transmit and receive polarisations are the same. In the following, the polarisations are constrained to the most commonly used orthogonal linear polarisations, the horizontal (H) and vertical (V). Each of the scattering coefficients, S_{pq}, are complex dimensionless numbers defining the power return in the associated receive (p) and transmit (q) channel where $p, q \in \{H, V\}$ [Lee and Pottier, 2009].

15

2.3.1 The Scattering Matrix

The *scattering matrix*, **S**, with horizontal and vertical polarisations inserted as the orthogonal basis is written as

$$\mathbf{S} = \begin{bmatrix} S_{HH} & S_{HV} \\ S_{VH} & S_{VV} \end{bmatrix} \in \mathbb{C}^{2x2}, \tag{2.5}$$

A radar system measuring the amplitude and phase of all four scattering coefficients is defined as a *fully polarimetric* or *quadrature polarisation* (quad-pol) radar [Raney, 2011]. For the linear horizontal and vertical case the four possible receive-transmit polarisation combinations are HH, HV, VH and VV. The combinations where the transmit and receive polarisation are equal are commonly referred to as the *co-pol* channels. Scattering coefficients of different receive and transmit polarisation are termed *cross-pol* channels. A *partially polarimetric* radar measures a subset of the scattering matrix, e.g., *single-pol* which comprises only one polarimetric channel, i.e., HH or VV, or *dual-pol* with two polarimetric channel combinations, e.g., HH and HV.

For a monostatic case where the same antenna is used for both transmitting and receiving, the scattering matrix is also known as the *Sinclair matrix* [Lee and Pottier, 2009].

2.3.2 The Scattering Vector

The scattering vector, $\vec{s}_C$, is the vectorised version of the scattering matrix in eq. (2.5). It is defined as,

$$\vec{s}_C = \begin{bmatrix} S_{HH} \\ S_{HV} \\ S_{VH} \\ S_{VV} \end{bmatrix} \in \mathbb{C}^{4x1}, \tag{2.6}$$

where the subscript C implies that this version of the scattering vector is utilised to calculate the polarimetric *covariance matrix*, given in eq. (2.8).

For monostatic configurations and for reciprocal propagation medium (targets whose internal state is not changing by the polarisation of the incident wave) the *reciprocity* theorem states that $S_{HV} = S_{VH}$ [Lee and Pottier, 2009]. However, in practice the HV and VH measurements are obtained at different times and through different receivers, thus thermal noise in the system will cause these numbers to be different. A common way to reduce the noise and get a more accurate value is to average these two channels, i.e., $S_{HV} = \frac{1}{2}(S_{HV} + S_{VH})$. The *reduced scattering vector* then becomes

$$\vec{s}_C = \begin{bmatrix} S_{HH} \\ \frac{1}{\sqrt{2}}(S_{HV} + S_{VH}) \\ S_{VV} \end{bmatrix} \in \mathbb{C}^{3x1}. \tag{2.7}$$

The term $\frac{1}{\sqrt{2}}$ ensures that the total scattered power is maintained, i.e.,

$$P_{tot} = Tr(\vec{s}_C \vec{s}_C^H) = |S_{HH}|^2 + |S_{HV}|^2 + |S_{VH}|^2 + |S_{VV}|^2,$$

where $Tr(A)$ represents the trace of the matrix A, and the operator $(\ )^H$ defines the Hermitian transpose operation.

Reciprocity is assumed to be valid for most naturally occurring terrain.

2.3.3 Covariance Matrix

From the original scattering vector in eq. (2.6) several useful matrices can be calculated. The most common is the *covariance matrix*, $\mathbf{C}$, which is calculated by averaging the outer product of L neighbouring scattering vectors, $\{\vec{s}_{C_i}\}_{i=1}^{L}$ as follows,

$$\mathbf{C} = \frac{1}{L} \sum_{i=1}^{L} \vec{s}_{C_i} \vec{s}_{C_i}^{H}. \tag{2.8}$$

The operation in eq. (2.8) is commonly known as *multilooking* (in the spatial domain). The polarimetric covariance matrix is positive definite and Hermitian symmetric and holds the multilook intensities of the polarimetric channels on the main diagonal. The off-diagonal contains the complex covariances of the channels.

All satellite scenes utilised in the presented work are acquired in a monostatic configuration and contain natural targets, i.e., sea ice and open water, hence the reciprocity principle is adopted in the equations presented in the succeeding paragraphs.

By inserting $\vec{s}_C$ from eq. (2.7) into eq. (2.8) we get

$$\mathbf{C_3} = \begin{bmatrix} \langle S_{HH}S_{HH}^* \rangle & \langle S_{HH}S_{HV}^* \rangle & \langle S_{HH}S_{VV}^* \rangle \\ \langle S_{HV}S_{HH}^* \rangle & \langle S_{HV}S_{HV}^* \rangle & \langle S_{HV}S_{VV}^* \rangle \\ \langle S_{VV}S_{HH}^* \rangle & \langle S_{VV}S_{HV}^* \rangle & \langle S_{VV}S_{VV}^* \rangle \end{bmatrix}. \tag{2.9}$$

The subscript 3 refers to the polarimetric dimension of $\vec{s}_C$ from which the covariance matrix is calculated. The operators $(\ )^*$ and $\langle \rangle$ denote the complex conjugation and computation of the sample mean, respectively.

The averaging in the multilook process may be performed using either a sliding or a stepping window. A sliding window is a technique, which moves the averaging window along the image. Prior to each averaging operation the window is shifted horizontally, or vertically, by one pixel. An illustration of the sliding window concept is provided in Fig. 2.4.

A stepping window operates in a similar way, but instead of shifting the window one pixel prior to each averaging, it is shifted the width of the window. A sliding window will blur the image, but preserve the total number of pixels, however, neighbouring pixels will be highly correlated. Using a stepping window causes the pixel resolution to degrade and reduces the total number of pixels. The latter may be preferable if the satellite scenes are big and thus, the processing slow. The covariance matrices utilised in the presented work are calculated using a stepping window.

In the following the covariance matrix may also be referred to as the C-matrix.
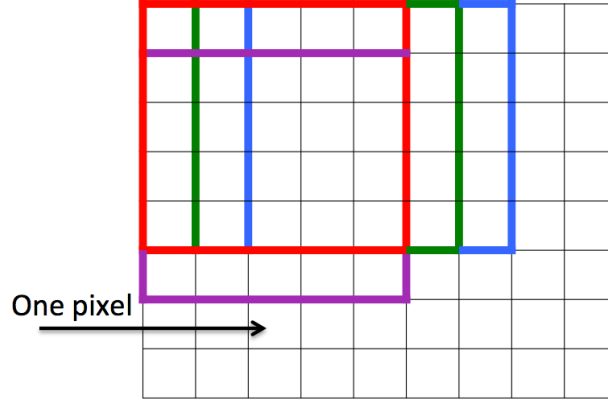
Figure 2.4: Illustration of the concept of a sliding window. Each black square represents one pixel. The red box represents the first pixel neighbourhood to be averaged. The green and the blue window represent the second and third neighbourhood to be averaged, respectively. Note that the windows have been slided, one pixel at a time, towards the edge of the image. The purple box is the first window at the second pixel row.

2.3.4   Polarimetric Decompositions

It is well-known that polarimetric SAR data carries information about the inherent scattering mechanisms of the illuminated area. Understanding the scattering mechanisms is one piece in the bigger picture of understanding the relationship between remotely sensed data and physical ice properties [Chen et al., 2014]. Polarimetric decompositions are in that respect a powerful tool to enhance the understanding of the underlying scattering mechanism and infer a physical interpretation of the target.

The basic idea of polarimetric decompositions is to decompose a measured polarimetric matrix into a summation of basic scattering mechanisms [Chen et al., 2014]. Therefrom, the dominant scattering mechanisms can be determined and physical parameters extracted. There are two primary groups of polarimetric decompositions, the coherent and the incoherent. The coherent decomposition theorems operate on the scattering matrix (eq. 2.5) and the incoherent decompositions on the covariance (eq. 2.8) or the coherency matrix (eq. 2.10). The latter is a simple linear transformation of the covariance matrix given by:

$$\mathbf{T_3} = \mathbf{U_3}\mathbf{C_3}\mathbf{U_3}^{-1} = \frac{1}{\sqrt{2}} \begin{bmatrix} 1 & 0 & 1 \\ 1 & 0 & -1 \\ 0 & \sqrt{2} & 0 \end{bmatrix} \mathbf{C} \begin{bmatrix} 1 & 0 & 1 \\ 1 & 0 & -1 \\ 0 & \sqrt{2} & 0 \end{bmatrix}^{-1} \tag{2.10}$$

where $\mathbf{C_3}$ is the covariance matrix given by eq. 2.8 and $\mathbf{U_3}$ is a special unitary transformation matrix [Lee and Pottier, 2009]. The subscript refers to the dimension of the

18

$\vec{s}_C$ from which the covariance matrix is calculated. In the decompositions employed in this thesis we have used the **C**-matrix. However, the incoherent decompositions yield equally valid results regardless of which matrix representation is used. The **T**-matrix representation has an advantage over the **C**-matrix due to its physical interpretation in terms of scattering mechanisms [Lee et al., 1999].

The work presented in this thesis is accomplished using parameters extracted from incoherent decompositions. There are two main categories of incoherent decompositions: eigenvalue-eigenvector-based decompositions and model-based decompositions [Lee and Pottier, 2009]. The eigenvalue-eigenvector-based decompositions have a clear mathematical background and only one unique solution. However, interpreting the result is complicated [Chen et al., 2014, van Zyl et al., 2011]. Contrarily, the result of a model-based decomposition is generally easier to interpret (often in terms of single-, double- or volume scattering, see Fig. 3.2), but with various combinations of scattering models it can produce different solutions [Chen et al., 2014]. For more details about the decompositions utilised in this thesis see section. 4.3.

Chapter 3

Remote Sensing of Arctic Sea Ice

The C-band wavelength is roughly equivalent to the dominant dimensions of the scatterers within the ice. Hence, C-band SAR is the preferred sensor for sea ice monitoring. The European remote sensing satellites Envisat, ERS-1 and -2 have together with RADARSAT-1 and -2 been the workhorses for providing C-band sea ice imagery. Of these, only the RADARSAT-2 is still in operation, but reached its minimum life expectancy of 7 years in 2014. In comparison the RADARSAT-1 satellite surpassed its life expectancy of 5 years after being operational for 17 years. A new space-borne SAR, the European Sentinel-1 [Torres et al., 2012] was launched in April 2014. It is currently in the operational qualification phase and the opening of the Sentinel-1 data flow to all users took place on October 3, 2014 [ESA Sentintel-1 Team, 2014].

3.1 Active Microwave Backscatter Properties of Sea Ice

In active microwave remote sensing the backscattering depends on the radar frequency, incidence angle, polarization, wavelength, instrumental noise and the scattering signatures of the illuminated area [Hallikainen and Winebrenner, 1992, Tucker III et al., 1992, Wackerman, 1992]. The latter will be affected by region, season and meteorological conditions, e.g., precipitation and wind, and is the combined effect of four physical parameters [Onstott and Shuchman, 2004], namely:

- the surface roughness,

- the relationship between radar viewing and surface geometry of the ice/snow,

- the complex dielectric constant (ϵ^*) of the sea ice,

- the existence of dielectric discontinuities or discrete scatterers, e.g., gas bubbles inside the ice.

The surface roughness is a measure of the deformation or unevenness of the illuminated surface. Whether a surface appears rough or not depends on the radar incidence angle

(θ), radar wavelength (λ) and the average height variations relative to a plane surface (Δh) [Onstott and Shuchman, 2004]. Height variations less than the radar wavelength will appear smooth to the radar. As the height variations increase, the illuminated area will appear rough. Fig. 3.1a illustrates the direction(s) of the reflected energy from a smooth surface. The backscattering from a rough surface is sketched in Fig. 3.1b. As most of the energy is reflected away from the radar by the smooth surface, such areas are identified by their dark appearance in satellite images. Contrarily, a rough surface acts as a diffuse scatterer, thus a significant fraction of the signal is backscattered towards the radar and hence will appear light on the radar image. The incidence angle will also affect the dark/light appearance of the illuminated surfaces. A steeper incidence angle causes more of the scattered energy to be backscattered in the direction towards the radar, hence an area will appear brighter (rougher) at steeper incidence angle, given that the frequency is unaltered.

The surface geometry of the ice caused by, e.g., ice blocks spread on the ice surface and pressure ridges, effects the large-scale surface roughness. Sea ice ridges with an orthogonal orientation with respect to the EM wave propagation will exhibit a strong double-bounce backscatter return (see Fig. 3.1c) to the radar. Ridges in parallel with the viewing direction of the radar reflect a weaker signal as the double-bounce reflections are limited to certain blocks within the ridge [Onstott and Shuchman, 2004].

The complex dielectric constant refers to the basic electrical properties of a material and determines the propagation, scattering, reflection and attenuation of the incident EM-wave [Onstott and Shuchman, 2004]. The complex dielectric constant is sometimes used interchangeably with the term electric permittivity. It is defined as:

$$\epsilon^* = \epsilon_0(\epsilon' - j\epsilon'') \tag{3.1}$$

where ϵ_0 is the free-space dielectric constant, ϵ' is the real part of $\frac{\epsilon^*}{\epsilon_0}$ and is referred to as the relative dielectric constant or relative permittivity, j is the complex unit and ϵ'' is termed the relative imaginary part or dielectric loss factor [Hallikainen and Winebrenner, 1992, Onstott and Shuchman, 2004]. The ϵ' governs the absolute backscatter level since the degree of scattering by a material is proportional to its dielectric constant. The dielectric loss factor controls the loss of energy in the medium, and hence the penetration depth of the EM-wave. Both the real and imaginary part of ϵ^* for ice and water depend on frequency, temperature and salinity. That is, lower frequencies penetrate to a greater extent, whereas ϵ^* increases with salinity and temperature [Onstott and Shuchman, 2004, Hallikainen and Winebrenner, 1992]. Water or wet snow on top of the ice act as an opaque filter to the radar wave and significantly reduces the penetration depth and prevents sensing of the ice surface. Contrarily, dry snow is highly transparent to microwave radiation [Sandven and Johannessen, 2006, Onstott and Shuchman, 2004].

The significantly increased microwave penetration depth in multiyear ice (see Table 3.1) compared to first year ice is due to its very low salinity. As the penetration depth

increases, a possible larger number of dielectric discontinuities, e.g., gas bubbles and brine inclusions, affect the backscattered signal. The inclusions and voids in multiyear ice are within an order of magnitude in size of the radar wavelengths at C- and X-band frequencies. Thus, multiyear ice under freezing conditions is dominated by volume scattering at C-band and higher frequencies [Onstott and Shuchman, 2004]. The principle of volume scattering is illustrated in Fig. 3.1d.

(a) **Single bounce/surface scattering** reflection off a specular/smooth surface. The reflection angle equals the incidence angle θ.

(b) Scattering off a rough surface. The surface height variation is in the order of the wavelength of the incoming signal.

(c) **Double bounce scattering** from a dihedral corner reflector.

(d) Example of **volume scattering** in snow. The incident wave is both reflected and refracted/transmitted through a layer of dry snow. The refracted wave is reflected from the underlined ice's surface, scatters off a chunk of ice in the snow, and is refracted back towards the radar.

Figure 3.1: Schematic models of radar backscattering. The black arrow on the left hand side of all subfigures illustrates the incident radar signal. The scattered signal is shown in red.

3.2 Sea Ice Types

Sea ice can be classified in terms of different parameters such as ice concentration or age. The work presented in this thesis is based on classification in terms of age, i.e., SoD as defined by the WMO [World Meteorological Organization, 2004]. A description of each ice type and its corresponding thickness is given in Table 3.1. The table is based on the description of WMO defined sea ice classes given in [MANICE, 2005, Ice Observation Handbook, 1984]. It should be noted that all thickness categories refers to level (undeformed) ice only.

In addition to the SoD of the ice, we have also considered its degree of deformation. The surface roughness variations are easily detected in SAR imagery, as radar backscatter provides good contrast between rough and smooth ice surfaces [Sandven and Johannessen, 2006] (see also chapter 3.1 and Fig. 3.2). Four different processes deform the ice: fracturing, hummocking, ridging and weathering [Onstott and Shuchman, 2004]. The fracture process ruptures and permanently deforms the ice, i.e., breaking across consolidated ice. Hummocking and ridging are pressure processes caused by converging ice sheets. The weathering process gradually eliminates irregularities on the ice surface by thermal and mechanical means.

According to the Ice Observing Handbook [Ice Observation Handbook, 1984] the surface of the ice can be divided into several categories. The most commonly referred categories are level ice, deformed ice, rafted ice, ridged ice, and hummocked ice. [Onstott and Shuchman, 2004]. Level ice is sea ice not yet deformed. Deformed ice is a general term for converging ice forced upwards, and downwards. Rafted, ridged and hummocked ice are subdivisions of deformed ice. Rafting entails the overriding of one piece of ice by another and occurs mostly on new and grey ice, thicker ice is more likely to ridge. Ridging occurs from compressional and shearing interactions of ice floes. Ridges are linear accumulations of ice and may rise several meters above and below the surface [Parmeter and Coon, 1972]. The part of the ridge above the surface is known as the "sail" and is shallower than the "keel" below the surface [Massom and Lubin, 2006a]. Deformed first-year ice may each a thickness of more than 20 meters [Ice Observation Handbook, 1984]. Hummocked ice is sea ice that has been piled haphazardly one piece over another [Ice Observation Handbook, 1984].

The SoD classification scheme is mainly based on a visual appearance of the ice. Hence, it is important to note that by means of radar, it is not possible to detect each SoD class. However, the radar provides additional information regarding surface conditions and structures of the ice [Dierking et al., 2004]. This information is especially useful when snow cover prevents optical imaging of the ice surface.

SoD	Properties	Thickness
New ice	General term for frozen seawater not yet solid ice	
Frazil ice	Collection of loose, randomly oriented needle-shaped ice crystals in water	
Grease ice	Thin soupy layer of ice crystals	
Slush	Slurry mixture of water saturated snow	
Shuga	Accumulation of spongy white ice with a diameter of a few centimeters	
Nilas	Consolidated ice, bends without breaking around waves and swells	$< 10\,\mathrm{cm}$
Dark nilas		$< 5\,\mathrm{cm}$
Light nilas		$5 - 10\,\mathrm{cm}$
Ice rind		$\sim 5\,\mathrm{cm}$
Young ice	Transition stage between nilas and first-year ice	$10 - 30\,\mathrm{cm}$
Grey ice	Less elastic than nilas, breaks on a swell. Usually rafts under pressure	$10 - 15\,\mathrm{cm}$
Grey-white ice	More likely to ridge than to raft under pressure	$15 - 30\,\mathrm{cm}$
First-year ice	Not more than one winter of age. Developing from young ice	$> 30\,\mathrm{cm}$
Thin first-year ice	Sometimes subdivided into: First stage Second stage	$30 - 70\,\mathrm{cm}$ $20 - 50\,\mathrm{cm}$ $50 - 70\,\mathrm{cm}$
Medium first-year ice		$70 - 120\,\mathrm{cm}$
Thick first-year ice		$> 120\,\mathrm{cm}$
Old ice	Ice that has survived at least one melting season	$\sim 2\,\mathrm{m}$
Second-year ice	Ice which has survived one melting season	
Multi-year ice	Ice which has survived more than one melting season	

Table 3.1: Stages of Development (SoD) of sea ice [MANICE, 2005, Smith, 2007].

25

(a) Frazil ice.
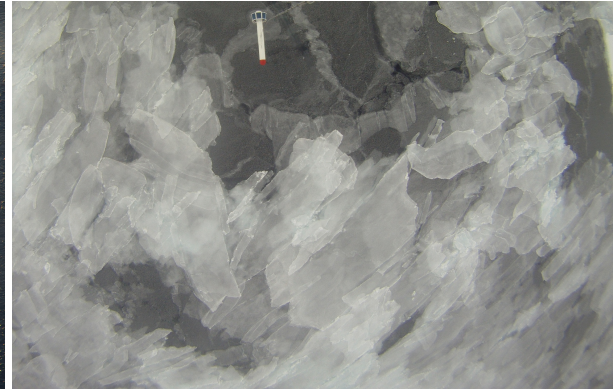
(b) Rafting nilas.

(c) Rafting nilas/grey ice.

(d) Arctic first-year ice.
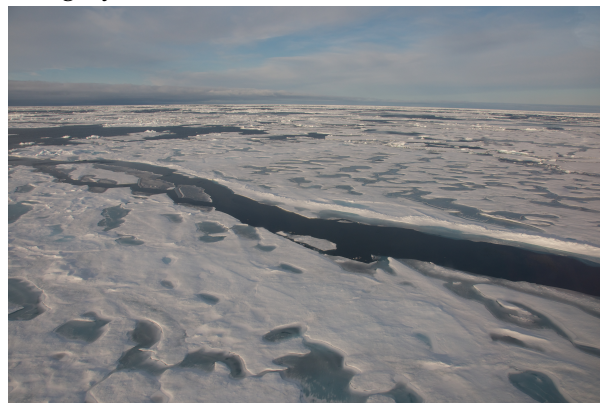
(e) Open lead and multiyear ice in late summer.

Figure 3.2: Examples of different ice types. Image courtesy of A. H. H. Renner, Norwegian Polar Institute.

3.3 Operational Sea Ice Charting

Ice services from several nations provide ice bulletins, warnings, analysis charts and forecasts. Primarily these are used to assist navigation in high-latitude waters where ice is present, but the products are increasingly used to support climate studies [Bertoia et al., 2004].

The geophysical ice parameters that are most important to the sea ice community comprise ice concentration, ice type, age, thickness, lead size and orientation, floe size, topography, ice drift, melt state and convergence/divergence conditions [Bertoia et al., 1998,WMO-No.574, 2010,Falkingham, 2014]. The major ice charting services of the Arctic use similar techniques. The differences are due to geographic regions of interest, user base and analysis data sets [Bertoia et al., 2004].

An example of a regional operational ice concentration chart covering the Svalbard area is shown in Fig. 3.3. The map is produced at the Ice Service of the Norwegian Meteorological Institute and is valid for September 12, 2014. The colours correspond to those defined by WMO in [World Meteorological Organization, 2004].

A sea ice forecaster handles a variety of data sources and manually fuses them into operational ice charts. Nowadays, the primary data source used for ice chart production is remote sensing image data. SAR instruments provide all-weather data with relatively frequent coverage and acceptable resolution for most applications, which are the principal reasons why SAR has become the sensor of choice [Falkingham, 2014]. Dual-pol (HH + HV or HH+VV) has become the standard polarimetric mode for operational ice classification [Falkingham, 2014]. In ScanSAR Wide mode RADARSAT can image every location on the Earth's surface north of 65°N latitude at least once every day [WMO-No.574, 2010]. In addition to SAR, other remote sensing instruments such as AVHRR (Advanced Very High Resolution Radiometer), MODIS (Moderate Resolution Imaging Spectroradiometer), SSM/I (Special Sensor Microwave/Imager) and QUIKS-CAT (Quick Scatterometer) are utilised [WMO-No.574, 2010,MANICE, 2005]. The satellite data are supplemented by airborne reconnaissance, ship reports, and meteorological and oceanographic information [Bertoia et al., 2004]. The fusion and interpretation process is time-consuming and the resulting charts are subject to the varying skills of the analysts [Falkingham, 2014,Moen et al., 2013a].

3.4 Automatic Sea Ice Classification from Polarimetric SAR Imagery

The Canadian Ice Service (CIS) alone processes ten to twelve thousand SAR images every year [Moen et al., 2013a]. Automating the whole or parts of the process has several advantages. First, automating the segmentation and/or the classification process increases the efficiency, hence making it achievable to process more data than what is currently managed. Secondly, the ice charts will be less dependent of the ice analyst's
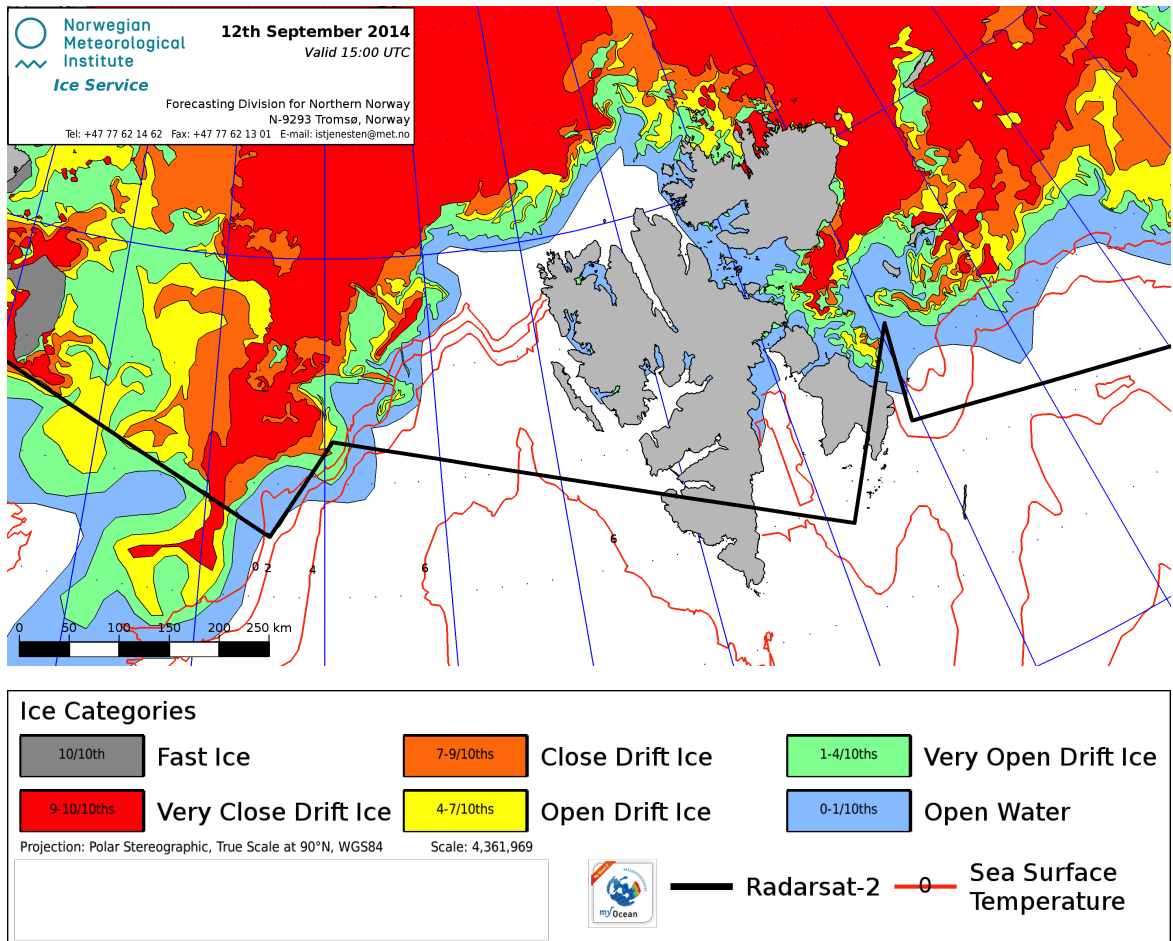
Figure 3.3: Regional operational ice concentration chart from the Svalbard region. Valid for September 12, 2014. Image courtesy of the Ice Service at the Norwegian Meteorological Institute.

education and experience [Moen et al., 2013a, Sephton and Partington, 1998]. Fig. 3.3 is an example of an operational ice chart. According to our definition this is a classification, because each colour represents a labelled ice category, which in this case corresponds to an ice concentration interval. Without the class labels (Fast ice, Open Water, etc.), we would have called it a segmentation.

Numerous different segmentation/classification algorithms exist and the categorisation of these is neither trivial nor obvious. In the context of sea ice segmentation/classification we find it meaningful to divide the algorithms along a number of axes, where each axis represents a subdivision into one of two groups. The categorisation of an algorithm involves labelling it with respect to each of these axes. The overall categorisation is not easily represented as a tree structure, as the branches will cross. The following subsections describe the axes. At the end of each subsection we state which group the

algorithms in our papers fall into.

3.4.1 Bayesian vs Non-Bayesian Decision Function

Bayesian segmentation/classification algorithms are those whose decision function is based on Bayes' theorem [Lee, 2012]. In Bayesian decision theory *a priori probabilities* are combined with class-conditional pdfs to arrive at conditional probabilities, also referred to as *posterior probabilities*. Bayes' rule can be expressed as

$$P(\omega_i|\vec{X}) = \frac{p(\vec{X}|\omega_i)P(\omega_i)}{p(\vec{X})}, \tag{3.2}$$

where $P(\omega_i|\vec{X})$ is the posterior probability, $p(\vec{X}|\omega_i)$ is the class-conditinal pdf, and $P(\omega_i)$ is the prior probability of class ω_i. The denominator, $p(\vec{X})$, is the pdf of $\vec{X}$. The Bayesian classification rule can be stated as follows:

$\vec{X}$ is assigned to ω_i if $\quad p(\omega_i|\vec{X}) > p(\omega_j|\vec{X}), \ \forall j \in \{1, .., N\} \neq i$

Non-Bayesian methods are complementary to the class of Bayesian methods, and can simply be defined as those whose decision function is not based on Bayes' theorem. All of our algorithms are Bayesian.

3.4.2 Supervised vs Unsupervised Learning

Both segmentation and classification algorithms deal with grouping of data points, and in our case pixels. A *supervised learning* problem is one, which exploits the a priori information given in a set of user-defined training data with known class labels. In an *unsupervised learning* problem, the groups in the data must be inferred from the data itself, without any knowledge of class labels indicated from training data. We have previously distinguished between the segmentation and classification tasks based on whether the resulting groups of pixels have class labels or not. According to this definition, a classification algorithm should be be categorised as supervised, since the resulting segments are labelled, which implies that labelled training data has been involved. Correspondingly, a segmentation method will be unsupervised, because the resulting segments have no class labels, and no training data is involved. Hence, it appears to be a one-to-one correspondence between the categories supervised versus unsupervised on one hand and classification versus segmentation on the other hand.
However, we have used methods where pixels are first grouped by an unsupervised segmentation algorithm and then labelled by use of expert knowledge rather than labelled training samples (Paper 1, ch. 6). This labelling could also be done by comparing the statistical characteristics of the unlabelled segments with those from a previous classification of a different data set. The labels could be assigned in order to obtain the best correspondence of class characteristics between the two classifications (according

to some criterion) (Paper 2, ch. 7). This would be done without the aid of labelled training sample and somewhat complicates the picture, which is why we choose to use the terms supervised/unsupervised in addition to classification/segmentation in order to describe our algorithms unambiguously.

The method utilised in Paper 1 (ch. 6) fall into the unsupervised learning category. In Paper 2 (ch. 7) we have used both supervised and unsupervised learning methods. The classification method exploited in Paper 3 (ch. 8) are categorised as a supervised learning method.

3.4.3 Parametric Modelling vs Non-Parametric Modelling

A classification/segmentation strategy based on parameterised families of probability distribution to model the underlying statistical distribution of the data is known as *parametric*. Contrarily, a *non-parametric* strategy requires no assumptions concerning the pdfs of the assessed variables. Non-parametric models differ from parametric models in that the pdf of the data is not specified a priori, but rather determined from the data itself. The reliance on fewer assumptions makes non-parametric models appropriate when less information about the data in question is available. In that sense non-parametric models are considered more robust. However, given that the prior assumptions in a parametric model are valid, its statistical power will exceed the one of a non-parametric model. In Paper 1 (ch. 6) and Paper 2 (ch. 7) we utilise parametric models. The non-parametric way of model the data is investigated in Paper 3 (ch. 8).

3.4.4 Gaussian Model vs Non-Gaussian Model

The Gaussian and Non-Gaussian categories are subcategories of the parametric modelling category [see 3.4.3]. All models based on the assumption that the complex scattering vector (see section 2.3.2, and eqs. (2.6) and (2.7)) is complex Gaussian distributed are assigned to the Gaussian model category. Violation of this assumption occurs for instance in high texture areas, or at very high resolutions. By textured areas we mean areas of heterogeneous radar reflectivity inside a class (e.g. ocean or forest). At very high resolutions, the number of scatterers inside each resolution cell is too small to justify the application of the central limit theorem. Segmentation/classification methods which do not assume Gaussian distributed scattering vectors are assigned to the non-Gaussian model category. Both Paper 1 (ch. 6) and Paper 2 (ch. 6) are classified into the Gaussian Model category.

3.4.5 Contextual vs Non-Contextual

Contextual segmentation/classification algorithms assign a given pixel to its segment/class by considering the information not only in the pixel itself, but also in its neighbourhood. As pixels are influenced by speckle (see section 2.1.1), the use of contextual in-

formation becomes particularly important. The speckle phenomenon leads to a large natural variability within segments/classes, which makes it very difficult to separate them in a feature-space based on the information in each pixel individually. A commonly used, and well-known contextual method is the Markov Random Field (MRF) method [Winkler, 2006]. Two different methods of contextual smoothing was applied to the segmentation performed in Paper 1 (ch. 6) and Paper 2 (ch. 7).

Chapter 4

Features for Sea Ice Discrimination

In the presented papers we test the sea ice discrimination of various features derived from the satellite data. Our selection of features includes features that: i) represent the main decomposition groups, ii) have shown sea ice segmentation/classification potential in previous studies, and iii) have not been used previously, but are considered promising candidates for sea ice segmentation/classification due to their physical interpretation. We divide the features into four main categories:

- features extracted directly from the C-matrix,

- features derived from the eigenvalues of the C-matrix,

- features calculated from polarimetric decompositions and statistical features,

- textural features, i.e., features calculated from a collection of pixels.

In the following we describe briefly each category and the features we have investigated in this thesis. We aim to also include a physical interpretation of each feature, however, some of the features do not have an obvious interpretation.

4.1 Features Extracted from the C-matrix Entries

Several features are extracted directly from the C-matrix (see ch. 2.3.3) or are ratios of the C-matrix elements.

4.1.1 Backscattering Coefficients/Intensities

The backscattering intensities from the different channels lie on the main diagonal of the C-matrix.

The backscattered **HH-intensity**, $I_{HH} = \langle S_{HH} S_{HH}^* \rangle$, of smooth surfaces decreases faster with increasing incidence angle than the VV-intensity. This makes the contrast between

rough and smooth level ice larger in the HH-channel [Dierking and Busche, 2006]. For operational monitoring HH-polarisation is the preferred single channel because ocean clutter is more suppressed than at VV-polarisation [Dierking and Pedersen, 2012, Partington et al., 2010, Scheuchl et al., 2004b].

For many ice types the co-pol channels are very similar [Onstott, 1992]. However, at high wind speeds the **VV-intensity**, $I_{VV} = \langle S_{VV} S_{VV}^* \rangle$, is better at discriminating several ice types over a wide range of incidence angles [Nghiem and Bertoia, 2001].

The **HV-intensity**, $I_{HV} = \langle S_{HV} S_{HV}^* \rangle$, is not sensitive to the incidence angle [Partington et al., 2010] and is relatively independent of wind-roughened water conditions compared to HH or VV [Scheuchl et al., 2001, Scheuchl et al., 2004b]. The HV backscatter from sea ice is sensitive to the surface roughness of the ice, and volume scattering [Scheuchl et al., 2004b]. Hence, it has potential in distinguishing younger ice from open water [Nghiem and Bertoia, 2001, Scheuchl et al., 2001], separating out deformed new ice [Arkett et al., 2008] and discriminating first-year from multi year ice [Nghiem and Bertoia, 2001, Arkett et al., 2008, Onstott, 1992].

4.1.2 Geometric Brightness

The geometric brightness (GB) is given as

$$GB = \sqrt[d]{det(\mathbf{C})}, \tag{4.1}$$

where d refers to the number of polarimetric channels in $\mathbf{C}$. In our case we have assumed reciprocity, hence $d = 3$. The geometric brightness is one way or representing the total power of the multichannel radar. It is the geometric mean of all channels. This feature is demonstrated to be sensitive to the illuminated target's roughness, geometric shape and orientation with respect to the radar [Paper 1, ch.6].

4.1.3 Span

The span represents the total power in the scattered field and is given by the trace of the covariance matrix [Drinkwater et al., 1992]:

$$\text{SPAN}\{\text{C}\} = Tr(\mathbf{C}). \tag{4.2}$$

The span is closely related to the geometric brightness feature in section 4.1.2. Hence the physical interpretation is also similar. The main difference is that the GB represent the total power based on a geometric mean, while SPAN{C} is proportional to the arithmetic mean. We include both the GB (section 4.1.2) and the SPAN{C} features to investigate which of these two has the best sea ice discrimination performance. In [Gill and Yackel, 2012] the authors demonstrated that the SPAN{C} is sensitive to both surface roughness and radar incidence angle. Deformed ice and open water had the highest SPAN{C} values, whereas smooth first-year ice had the lowest values.

4.1.4 Co-polarisation Ratio

The co-polarisation ratio is given by

$$R_{VV/HH} = \frac{\langle S_{VV}S_{VV}^* \rangle}{\langle S_{HH}S_{HH}^* \rangle}. \tag{4.3}$$

Its value is determined by the dielectric constant of the surface. In [Scheuchl et al., 2001] the co-polarisation ratio, $R_{VV/HH}$, proved to be useful for separating open water from thin-ice types. First-year and multi-year ice have values of ~ 1. Open water and new ice have the largest observed values [Onstott and Shuchman, 2004]. The study performed by Gill and Yackel [Gill and Yackel, 2012] reports very high variability in co-polarisation ratio for all ice types represented. This hampers its sea ice discrimination potential. However, it was shown useful for ice-water separation.

4.1.5 Cross-polarisation Ratio

The cross-polarisation ratio is given by

$$R_{HV/GB} = \frac{\langle S_{HV}S_{HV}^* \rangle}{GB}. \tag{4.4}$$

In our work we define the cross-polarisation ratio slightly different than other studies, i.e., as the ratio of cross-pol intensity to geometric brightness. The cross-polarisation ratio estimates the amount of depolarisation. The cross-polarisation ratio has proven useful for distinguishing between ice types and estimating ice age. The CIS has identified several situations where combining dual-pol channels may aid an ice analyst. These are; detection of old ice (when embedded in first year ice), separation between open water and ice, lead detection, and estimating ice concentration [Scheuchl et al., 2004a].

4.1.6 Co-polarisation Correlation Coefficient

The co-pol correlation coefficient, ρ, is a complex number. Hence both the magnitude and phase, or the real and imaginary parts may contain useful information [Doulgeris, 2013]. ρ is calculated as follows [Drinkwater et al., 1992]:

$$\rho = \frac{\langle S_{HH}S_{VV}^* \rangle}{\sqrt{\langle S_{HH}S_{HH}^* \rangle \langle S_{VV}S_{VV}^* \rangle}}. \tag{4.5}$$

Previous studies have utilised the magnitude, $|\rho|$, and the phase, $\angle\rho$, in sea ice studies [Kwok et al., 1998, Drinkwater et al., 1992, Gill and Yackel, 2012, Doulgeris, 2013, Moen et al., 2013a]. Using the phase and magnitude representation of the co-pol correlation coefficient in clustering analysis should be performed with awareness of to the possible

phase wrapping [Doulgeris, 2013].

The interpretation of $|\rho|$ in terms of sea ice types is yet to be determined [Onstott and Shuchman, 2004]. However, [Drinkwater et al., 1992] indicated that it relates to both salinity and incidence angle. The results presented in [Gill and Yackel, 2012] show that $|\rho|$ decreases with incidence angle and with ice deformation. Open water had the largest values of $|\rho|$.

The co-polarisation correlation phase has been demonstrated to be useful for classification, as a proxy in thickness estimation of thin ice types (i.e., $< \sim 0.3$m) [Thomsen et al., 1998a, Thomsen et al., 1998b], and also to separate open water from ice. Its value is determined by the water and ice dielectric constants, with the largest angle for new ice [Onstott and Shuchman, 2004].

4.2 Eigenvalue-Based Features

The special unitary transformation matrix (see 2.10) relates the covariance matrix and the coherency matrix. Hence, their eigenvalues are identical [Lee and Pottier, 2009] and the following features can be derived from either of the matrices.

4.2.1 Eigenvalues

By definition, if A is an $n \times n$ matrix, a real number λ_i is called an *eigenvalue* of A if

$$A\vec{u}_i = \lambda_i \vec{u}_i. \tag{4.6}$$

The vector $\vec{u}_i$ is called an *eigenvector* of A [Nicholson, 1995]. In our case A is the 3×3 covariance matrix, hence $i = \{1, 2, 3\}$.

The C-matrix may be decomposed into the sum of three independent targets as follows:

$$\mathbf{C}_3 = \sum_{i=3}^{3} \lambda_i \vec{u}_i \vec{u}_i^H \tag{4.7}$$

If only one of the eigenvalues is nonzero, the covariance matrix corresponds to a pure target. Another extreme case is a covariance matrix made up of three different scattering mechanisms, i.e., $\lambda_1 = \lambda_2 = \lambda_3 \neq 0$. This type of covariance matrix represents a completely de-correlated, non-polarised random scattering structure. The partially polarised scatterers (nonzero and nonequal eigenvalues) occur between these two extremes [Lee and Pottier, 2009].

4.2.2 Pedestal Height

The Pedestal Height (PH) is a measure of the unpolarised scattering component in the average returned signal and thus the degree of polarispolarisation of a scattered wave

[Lee and Pottier, 2009, Jiao et al., 2011]. PH is calculated as follows:

$$PH = \frac{min(\lambda_1, \lambda_2, \lambda_3)}{max(\lambda_1, \lambda_2, \lambda_3)} = \frac{\lambda_3}{\lambda_1}, \quad \lambda_3 \leqslant \lambda_2 \leqslant \lambda_1, \tag{4.8}$$

where λ_i is the ith eigenvalue of the polarimetric covariance matrix given in eq.(2.8).Targets dominated by volume scattering or multiple-surface scattering are typical for signatures with significant PH values [Jiao et al., 2011]. Several studies have demonstrated that the PH increases with surface roughness [Hossain, 2012, Gill et al., 2010], [Paper 3, ch. 8].

4.2.3 Polarisation Fraction

The definition of the polarisation fraction (PF) is given by

$$PF = 1 - \frac{3\lambda_3}{\text{SPAN}\{C\}} = 1 - \frac{3\lambda_3}{\lambda_1 + \lambda_2 + \lambda_3}, \quad \lambda_3 \leqslant \lambda_2 \leqslant \lambda_1. \tag{4.9}$$

The subtrahend represents the fraction of the completely unpolarised power ($3\lambda_3$) of the total power ($Span_{C_3}$). The remaining power corresponds to the polarised fraction of the signal [Lee and Pottier, 2009]. The maximum PF value occurs when the entire backscattered signal is polarised, i.e., $\lambda_3 = 0$.

4.2.4 Polarisation Asymmetry

The polarisation asymmetry (PA) is defined as the fraction of the difference and sum of the polarised part (unpolarised part, λ_3, is removed) of the two largest eigenvalues:

$$PA = \frac{(\lambda_1 - \lambda_3) - (\lambda_2 - \lambda_3)}{(\lambda_1 - \lambda_3) + (\lambda_2 - \lambda_3)} = \frac{\lambda_1 - \lambda_2}{\text{SPAN}\{C\} - 3\lambda_3}, \quad \lambda_3 \leqslant \lambda_2 \leqslant \lambda_1. \tag{4.10}$$

The PA is a measure of the relative strength of the two polarised scattering mechanisms [Lee and Pottier, 2009].

4.3 Features from Polarimetric Decompositions

The following subsections provide a brief summary of the different polarimetric decompositions we have used in the presented work. See section 2.3.4 for general information about polarimetric decompositions.

4.3.1 The H/A/α Decomposition

The H/A/α decomposition [Cloude and Pottier, 1997] is a decomposition based on the eigenvalues and eigenvectors of the **T**-matrix and does not rely on the assumption of

particular underlying statistical distribution [Lee and Pottier, 2009]. The polarimetric scattering entropy (H) is a statistical measure of the randomness of the scattering process. In our case of a 3×3 coherency matrix, the entropy is defined as:

$$H = -\sum_{i=1}^{3} P_i \log_3 P_i, \tag{4.11}$$

where P_i corresponds to the pseudo-probabilities obtained from the eigenvalues λ_i:

$$P_i = \frac{\lambda_i}{\sum_{i=1}^{3} \lambda_i} \tag{4.12}$$

In the extreme case when $H = 1$, all eigenvalues are equal, and the scattering process is completely random. A high entropy value means that the target is represented by more than one scattering mechanism and they are equal in strength. A depolarising surface is characterised by a non-zero entropy value. Low values of H indicate that the target is dominated by a single scattering mechanism, i.e., a weakly depolarising scattering process. Results presented in [Gill and Yackel, 2012] indicate that H increases with increasing surface roughness.

The polarimetric anisotropy feature (A) is a complementary parameter to the entropy. It is defined as the relative importance of the second and the third eigenvalue:

$$A = \frac{\lambda_2 - \lambda_3}{\lambda_2 + \lambda_3}, \ \lambda_3 < \lambda_2 < \lambda_1. \tag{4.13}$$

At high entropy values the number of distinguishable classes identifiable from polarimetric observations reduces. In such cases the anisotropy becomes useful as it improves the capability to distinguish different types of scattering processes. At lower entropy values λ_2 and λ_3 and consequently the anisotropy are highly affected by noise [Lee and Pottier, 2009]. The anisotropy is independent of the dielectric constant and sensitive to surface roughness [Schuler and Lee, 2006, Hajnsek et al., 2003]. In the investigation performed by [Gill and Yackel, 2012], the anisotropy was able to clearly separate the smooth first-year ice class from the other ice classes.

Each of the eigenvectors of the coherency matrix can be expressed in terms of five angles [Cloude and Pottier, 1997]. In the presented work we have only evaluated the sea ice discrimination power of the α angle. The α parameter is extracted from the eigenvectors given by the following equation

$$\vec{u}_i = [\cos \alpha_i \quad \sin \alpha_i \cos \beta_i \exp(j\delta_i) \quad \sin \alpha_i \sin \beta_i \exp(j\gamma_i)]^T, \tag{4.14}$$

where $\vec{u}_i$ is the ith normalised eigenvector of the coherency matrix. The target's absolute phase has been ignored. From equation 4.14 we get three α values, i.e., α_1, α_2 and α_3. These values are averaged according to eq. 4.15 to get the averaged α parameter.

$$\overline{\alpha} = \sum_{i=1}^{3} P_i \alpha_i, \ 0° \leqslant \overline{\alpha} \leqslant 90°, \tag{4.15}$$

where α_i is derived from eq. (4.14) and P_i from eq. (4.12). The $\overline{\alpha}$ parameter indicates the "type" of the average dominant scattering process occurring. Low $\overline{\alpha}$ values are interpreted as single bounce scattering/surface scattering ($0° \leqslant \overline{\alpha} \leqslant 40°$). Values ranging from $\sim 40°$ to $\sim 53°$ are interpreted as volume scattering. The remaining region, $53° \leqslant \overline{\alpha} \leqslant 90°$ determines the span where double bounce scattering occurs [Lee and Pottier, 2009].

4.3.2 The Target Scattering Vector Model (TSVM)

The parameters from the target scattering vector model (TSVM) [Touzi, 2004, Touzi, 2007] are calculated from the eigenvectors of the coherency matrix (eq. 2.10). The eigenvectors of the **T**-matrix can be expressed in terms of five parameters ($\Phi_s, \alpha_s, \tau_m, \psi_s$ and Φ_{α_s}):

$$\vec{u}_i^{TSVM} = \exp(j\Phi_s) \begin{bmatrix} \cos\alpha_{si}\cos\tau_{mi} \\ -j\cos\alpha_{si}\sin 2\psi_{si}\sin 2\tau_{mi} + \cos 2\psi_{si}\sin\alpha_{si}\exp(j\Phi_{\alpha_s}) \\ -j\cos\alpha_s\cos 2\psi\sin 2\tau_m + \sin 2\psi\sin\alpha_s\exp(j\Phi_{\alpha_s}) \end{bmatrix}. \quad (4.16)$$

The $\vec{u}_i^{TSVM}$ is a normalised eigenvector. The subscript i refers to the ith eigenvector, $i \in \{1, 2, 3\}$. The four parameters, α_s, τ_m, ψ_s and Φ_{α_s} describe the magnitude, helicity, orientation angle and phase of the maximum polarisation response, respectively [Touzi, 2007]. They are extracted from the eigenvectors of the **T**-matrix using eq. (4.16). We have ignored the absolute phase of the target, Φ_s, since we are not doing interferometry [Touzi, 2007]. The overline, $\overline{(\;)}$, denotes the averaged parameter calculated as described in eq. (4.15).

The study performed by [Gill and Yackel, 2012] investigated the classification potential of the TSVM parameters. From the class-wise pdfs plotted together for each parameter they concluded as follows. The ψ parameter is able to separate open water and deformed first-year ice, the other classes are mixed. Utilising the τ_m, ϕ_s or the α_s, open water can be separated from the other ice classes.

4.3.3 The Non-Negative Eigenvalue Decomposition (NNED)

The non-negative eigenvalue decomposition (NNED) [van Zyl et al., 2011] is a hybrid approach involving model-based and eigenvalue-based decomposition. This decomposition was developed for decomposing SAR scenes of vegetated terrain into different scattering components. The NNED ensures that all covariance matrices in the decomposition have real and non-negative eigenvalues [van Zyl et al., 2008, van Zyl et al., 2011], which is a significant flaw in several other model-based decompositions such as the decompositions proposed by Freeman and Durden [Freeman and Durden, 1998] and Yamaguchi et al. [Yamaguchi et al., 2005].

The general idea is to separate the covariance matrix into a linear combination of three model matrices. Each model matrix represents a predefined scattering type. Common scattering types are single-bounce, double-bounce and volume scattering (see Fig.

3.2). The first step in the NNED is to subtract a covariance matrix representing a proportion, c^{col}, of the model for volume scattering, $\mathbf{C}^{\mathrm{vol}}$, from the observed covariance matrix, $\mathbf{C}$:

$$\mathbf{C}^{\mathrm{rem}} = \mathbf{C} - c^{\mathrm{vol}}\mathbf{C}^{\mathrm{vol}}. \tag{4.17}$$

The superscripts vol and rem indicates whether the matrix represents the volume component or the remainder covariance matrix, respectively. The latter will contain whatever is in the observed matrix $\mathbf{C}$ that is not consistent with the subtracted proportion of the volume model matrix. The factor c^{vol} is chosen such that all the represented covariance matrices are physically realisable, which means all eigenvalues must be real and greater than or equal to zero. Given that the $\mathbf{C}^{\mathrm{vol}}$ is given by [Freeman and Durden, 1998]:

$$\mathbf{C}^{\mathrm{vol}} = \begin{bmatrix} 1 & 0 & \frac{1}{3} \\ 0 & \frac{2}{3} & 0 \\ \frac{1}{3} & 0 & 1 \end{bmatrix}, \tag{4.18}$$

it can be shown [van Zyl et al., 2011] that the maximum value of c^{vol} is given by

$$c^{\mathrm{vol}} = \min \begin{cases} \frac{3}{2}\mathbf{C}_{22}^{\mathrm{vol}} \\ \frac{9}{16}(a - \sqrt{a^2 - b}) \end{cases}, \tag{4.19}$$

where

$$a = \mathbf{C}_{11}^{\mathrm{vol}} + \mathbf{C}_{33}^{\mathrm{vol}} - \frac{2}{3}Re\{\mathbf{C}_{12}^{\mathrm{col}}\}$$
$$b = \frac{32}{9}(\mathbf{C}_{11}^{\mathrm{vol}}\mathbf{C}_{33}^{\mathrm{vol}} - |\mathbf{C}_{13}^{\mathrm{vol}}|^2)$$
.

The subscripts refer to the corresponding row and column entries in the covariance matrix. The remainder covariance matrix after the volume term has been subtracted is decomposed using the eigenvector decomposition. This can be expressed mathematically as [van Zyl et al., 2011]:

$$\langle[\mathbf{C}]\rangle = c^{vol}[\mathbf{C}^{\mathrm{vol}}] + \lambda^{\mathrm{sgl}}[\mathbf{C}^{\mathrm{sgl}}] + \lambda^{\mathrm{dbl}}[\mathbf{C}^{\mathrm{dbl}}] + \lambda^{\mathrm{rem}}[\mathbf{C}^{\mathrm{rem}}]. \tag{4.20}$$

The lambdas represent the eigenvalues of the corresponding covariance matrices. The superscripts vol, sgl and dbl indicates which scattering mechanism it represents; volume, single-bounce or double-bounce. The last matrix on the right, $\mathbf{C}^{\mathrm{rem}}$, can be considered the remaining after the volume, single-bounce and double-bounce terms have been subtracted. In general, this matrix will include additional cross-polarised power possibly occurring from terrain effects and rough surface scattering [van Zyl et al., 2011].

In paper 3 [see Ch. 8], we evaluated the classification power of three intensities. The remainder part was ignored. The intensities are calculated from each of the covariance matrices as follows:

$$I^{\mathrm{vol}} = Tr\{c^{\mathrm{vol}}\mathbf{C}^{\mathrm{vol}}\}$$
$$I^{\mathrm{sgl}} = Tr\{\lambda^{\mathrm{sgl}}\mathbf{C}^{\mathrm{sgl}}\} . \tag{4.21}$$
$$I^{\mathrm{dbl}} = Tr\{\lambda^{\mathrm{dbl}}\mathbf{C}^{\mathrm{dbl}}\}$$

The dominant scattering mechanism in SAR scenes comprising sea ice is generally surface scattering. Areas of significant double-bounce scattering are interpreted as broken up sea ice because of the occurring corner configurations (see Fig. 3.1c). In our first-year ice scenes, volume scattering appears in areas of deformed ice [Moen et al., 2013b].

4.4 Textural Features

The textural feature utilised in our work is a measure of statistical properties calculated from a neighbourhood of pixels.

4.4.1 Relative Kurtosis

The Relative Kurtosis (RK) is a statistical quantity that measures the shape of a distribution relative to a Gaussian distribution. The RK is given by [Doulgeris, 2013]

$$\frac{1}{RK} = \frac{L d_{\vec{s}}(d_{\vec{s}} + 1)}{\sum_{i=1}^{L} \left[\vec{s}_i^H \mathbf{C}^{-1} \vec{s}_i\right]^2}. \tag{4.22}$$

L, $\vec{s}_i$ and C correspond to the quantities used in eq. (2.8). $d_{\vec{s}}$ is the number of elements in the $\vec{s}_i$-vector. The sea ice classification power of this feature has not previously been investigated. Our studies demonstrated that the RK feature is sensitive to sea ice deformation. Highly deformed ice, such as ice edges, ridges and rubble fields create few, but strong reflections. Hence, the Gaussian assumptions are violated and the values of the RK become large. Areas with intensity differences due to mixture components, i.e., inhomogeneous areas, will also have increased RK values [Paper 1, ch. 6].

Chapter 5

Study Area and Data Material

5.1 Study Area

The presented work utilises various sea ice data collected during a research cruise with the Norwegian coastguard vessel "Svalbard" north of Svalbard in April 2011 (see Fig. 5.1). The remote location in combination with frequent harsh weather conditions makes this a challenging area to work in. The region composed of open and refrozen leads and drifting first-year ice at various stages of development [Moen et al., 2013a, Renner et al., 2013].

5.2 Satellite Data

All satellite scenes employed in the following papers are RADARSAT-2 quad-pol scenes acquired from the 6 April to the 13 April 2011. Figure 5.1 illustrates the location of each scene and the position of the vessel on the 12 April. All scenes are acquired in standard fine quad-pol mode at ascending pass direction. More details about the scenes utilised in this thesis is given in table 5.1. All RADARSAT-2 scenes are provided by the Norwegian Space Centre (NSC)/Kongsberg Satellite Services (KSAT) under the Norwegian/Canadian RADARSAT agreement 2011.

Date	Time (UTC)	Centre Position	CIA	GRR	GAR
11 April 2011	14:04	81.0911°N 19.4561°E	24.358°	11.5 m	5.0 m
12 April 2011	15:15	81.1228°N 19.8664°E	40.048°	7.4 m	4.9 m
13 April 2011	14:46	81.1578°N 19.7469°E	33.262°	8.6 m	4.7 m

Table 5.1: Information about the satellite scenes. CIA is the Centre Incidence Angle, GRR is the Ground Range Resolution and GAR is the Ground Azimuth Resolution.
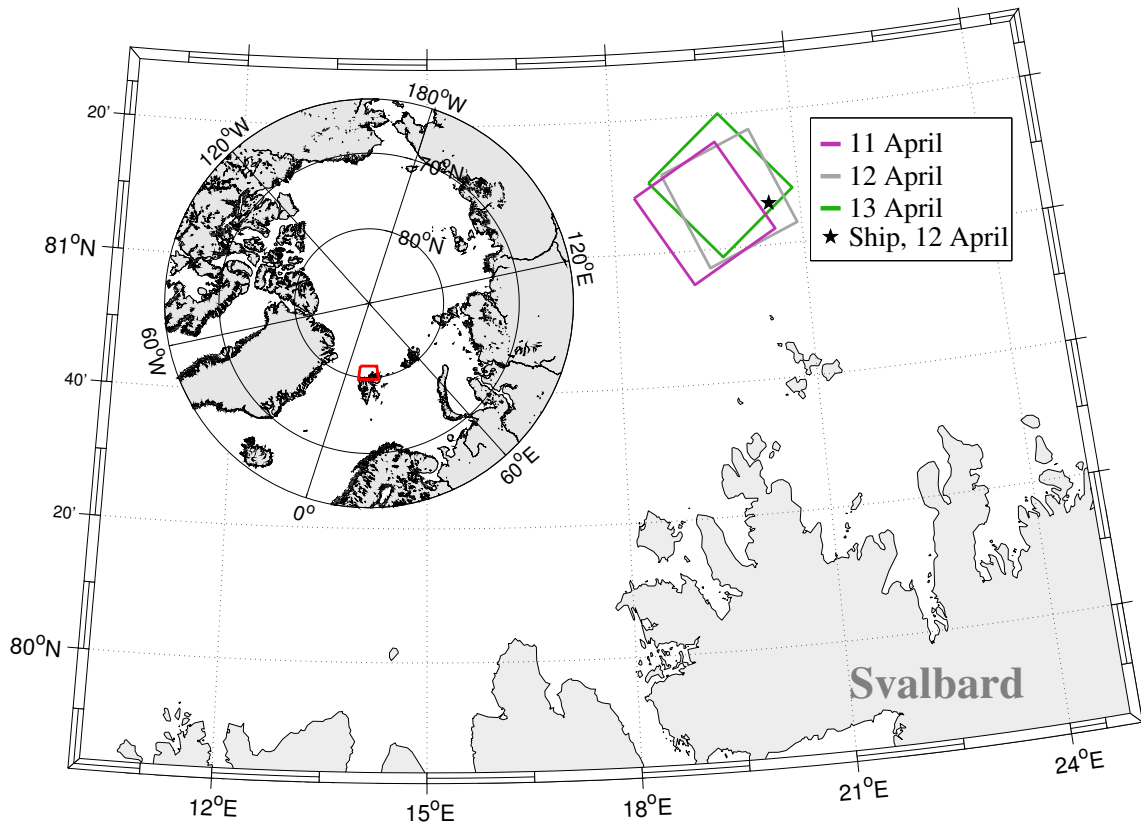
Figure 5.1: Section of the northern hemisphere showing the geographical location of the quad-pol scenes used in the papers presented in this thesis. The red box inside the circular map shows the location of the area shown in the largest map. The individual positions of the scenes are shown as coloured boxes north of Svalbard. The black star is the position of the ship on 12 April 2011.

5.3   In-Situ Measurements

In-situ measurements remain crucial for validation of models and for understanding geophysical processes. Field data are also used to validate or calibrate satellite derived sea ice parameters. Hence, remotely sensed data are complementing rather than replacing in-situ measurements in the sea ice zone [Eicken et al., 2009]. Various snow and sea ice in-situ measurements were collected during the April 2011 cruise. Only measurements exploited in the presented papers are described in the following paragraphs.

5.3.1   Ship-Based Sea Ice Observations

Sea ice observations and accompanying photos were collected regularly from the "Svalbard's" bridge. This dataset contains information about the vessel's position and speed, ice types, ice concentration, floe sizes, rafting and ridging of the ice, air temperature, water temperature, wind speed and direction, humidity and cloud-cover.

5.3.2 Electromagnetic Induction Sounder

On 12 April an electromagnetic induction sounder was towed above the ice by a helicopter, a sensor commonly known as EM-bird. The EM-bird measures the total snow and ice thickness averaged over the footprint of the EM-bird ($\sim 40 - 50$ m). The principle of the EM-bird thickness measurements is described in detail by [Haas et al., 2009], thus only a brief description of the method will be provided here.
EM sea ice thickness sounding exploits the large difference in electrical conductivity of sea ice and seawater. A transmitting coil generates a primary EM field, which induces eddy currents in the seawater under the ice. These eddy currents generate a secondary EM field whose strength is measured by the receiving coil of the EM system. The strength of the induced secondary EM field is directly related to the distance h_w between the EM instrument and the seawater surface, i.e., the ice-water interface. The distance h_i from the EM-bird to the top of the ice (top of the snow in case of snow-covered sea ice) is provided by a laser altimeter mounted in the EM-bird. The total ice thickness, i.e., the sum of snow plus ice thickness, Z_i, follows from the difference between the distances h_w and h_i, see Eq. 5.1. Over level sea ice the EM-bird accuracy is found to be within ± 0.1 m of drill-hole validation measurements [Haas et al., 2009].

$$Z_i = h_w - h_i \tag{5.1}$$

Thickness measurements using an airborne EM system make it possible to retrieve thickness measurements over much larger and inaccessible areas than with the hole-drilling method. Figure 5.2a and 5.2b show the EM-bird in operation and a close-up, respectively.

5.3.3 Optical Photos from Helicopter Flights

The helicopter flew in a butterfly-like pattern to cover as much as possible of the corresponding satellite scene (see the frontpage of the thesis or Fig. 2(a) in Paper 1, ch. 6). To get coinciding photographs with the thickness measurements an optical GoPro down-looking camera was mounted on the helicopter's chassis.

5.3.4 Global Positioning System Trackers

An additional means of quantifying the sea ice drift was gained by deploying Garmin Global Positioning System (GPS) trackers. On the 12 April a GPS transmitter (Garmin DC-40 collar) was flown out to an ice floe. Onboard the ship the GPS receiver (Garmin Astro 220 with Astro portable long range antenna) obtained the collar positions every 30 seconds on average. The ice drift measurements were used to calculate the ice drift between the satellite scene acquisition and the EM-bird flight. Fig. 5.2c displays how the GPS tracker was deployed on the ice.

5.3.5   Iridium Surface Velocity Profiler Buoy

An Iridium Surface Velocity Profiler (ISVP) buoy from Metocean was deployed onto an ice floe on 11 April. Every hour the buoy transmits its position together with other parameters such as barometric pressure and sea surface temperature. The positions can be used to calculate the ice drift in the buoy's vicinity. Fig. 5.2d shows the ISVP buoy deployed on the ice.
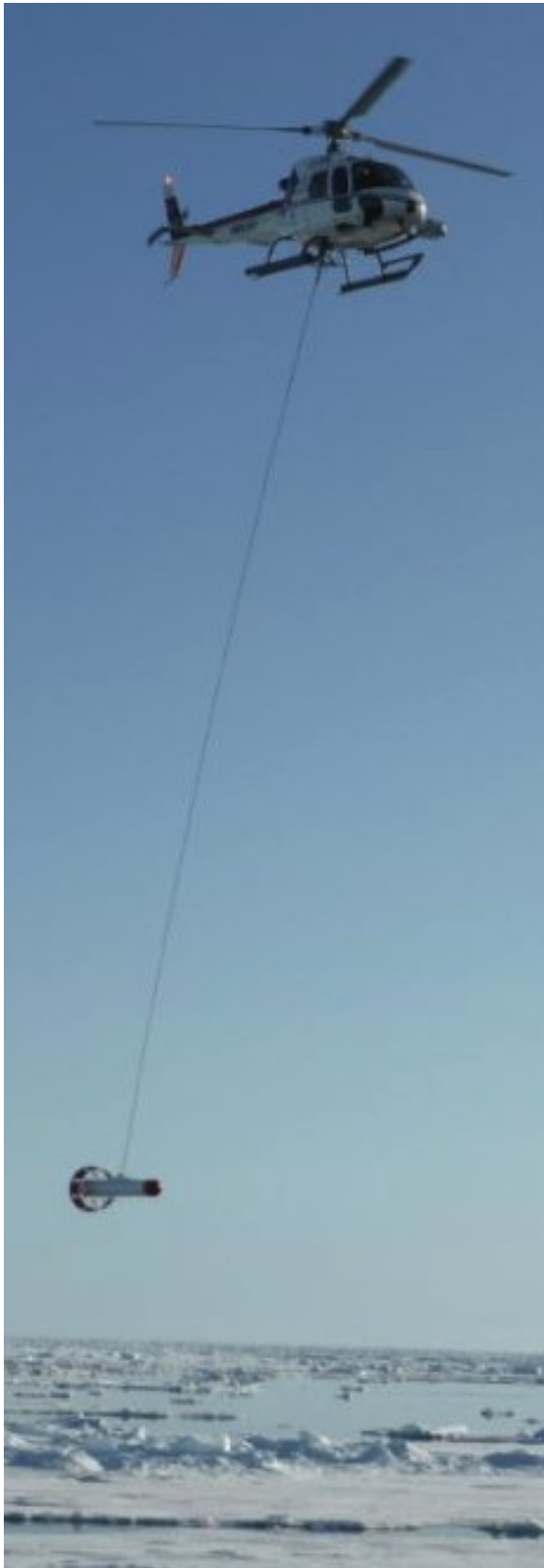
(a) EM-bird flight. Image courtesy of S. Gerland, Norwegian Polar Institute.

(b) Close-up of EM-bird. Image courtesy of A. H. H. Renner, Norwegian Polar Institute.

(c) GPS tracker mounted on a wooden stick. Image courtesy of S. Gerland, Norwegian Polar Institute.

(d) Iridium Surface Velocity Profiler (ISVP) buoy. Image courtesy of S. Gerland, Norwegian Polar Institute.

Figure 5.2: Instruments for in-situ measurements.

Chapter 6

Paper 1: Comparison of feature based segmentation of full polarimetric SAR satellite sea ice images with manually drawn ice charts

Chapter 7

Paper 2: An inter-comparison of techniques to classify polarimetric SAR images of sea ice

Chapter 8

Paper 3: Optimal Feature Combination for Segmentation and Classification of sea ice SAR images

Chapter 9

Conclusions

The papers presented in chapters 6 - 8 add to the on-going research of polarimetric SAR imagery for sea ice related applications, sea ice segmentation and classification in particular. This chapter provides a summary of our research conclusions, point out challenges that still are unsolved, and includes some ideas for future research.

9.1 Concluding Remarks

Various sea ice segmentation and classification methods have been tested on SAR scenes of sea ice. In this thesis we investigate segmentation and classification algorithms based on polarimetric features derived from quad-pol RADARSAT-2 scenes.

In Paper 1 (ch. 6), we have focused on efficient methods for ice chart production. We demonstrated that manually drawn sea ice charts were highly dependent on the ice analyst producing the charts. Manually made ice charts depend crucially on the experience and education of the ice analyst. Such ice charts are commonly used for validation of various automatic classification algorithms [Zakhvatkina et al., 2013, Kwon et al., 2013]. Our investigation showed that it is important to consider the subjectivity of the stage of development (SoD) ice charts when such charts are applied for validation purposes.

Both studies performed in Paper 1 and Paper 2 (ch. 7) showed that the segments produced by the utilised feature based unsupervised automatic algorithm were reasonable, and could be interpreted using polarimetric features with a clear physical interpretation. In Paper 1 we utilised a parameter, the relative kurtosis (RK), which had previously not been used for sea ice segmentation and/or classification purposes. The RK parameter is a statistical measure of the shape of a distribution relative to a Gaussian distribution and can be linked to roughness or heterogeneity in the radar reflectivity. Our survey confirmed that the RK parameter is related to the sea ice surface roughness and are useful for both segmentation and subsequent class labelling.

The polarimetric parameters are not expected to be invariant through seasonal changes.

This is one reason no automatic methods for sea ice classification from SAR images are robust enough to be used all year round. Some features are also sensitive to variations in incidence angle. Thus, the interpretation of the polarimetric signature of classes in one scene may not be directly transferrable to other scenes. In Paper 2, we addressed the issue of transferability of information between scenes by investigating three scenes from consecutive days with slightly different incidence angles. The data set is limited both in time and space, hence definite conclusions are not drawn.

A good incidence angle correction is essential prior to scene comparisons. The incidence angle correction applied in Paper 2 is performed by multiplying a correction factor to the scattering vectors. The correction factor is the square root of the ratio of the sine of the centre incidence angle to be corrected, and the sine of the centre incidence angle of the reference scene. This type of correction will not effect all types of features as some are ratios of covariance matrix elements, and hence the correction factor will vanish. Our investigation revealed that the performed incidence angle correction effected the ice classes differently and it is not a sufficient correction, especially when the incidence angle difference between the scenes is large.

The scenes are individually segmented utilising an unsupervised automatic method. These segmentations look reasonable. Two of the segmented images are classified using the third as reference. The reference scene has the largest incidence angle. The labelling is performed by testing various statistical distance measures. We concluded that the Mahalanobis distance measure is the best performing distance measure. The scene with the smallest incidence angle deviation from the reference scene is labeled identical to the manually performed labelling. Five of seven classes are perfectly matched for the scene with the steepest incidence angle. A supervised pixel-wise classification method, which utilise the feature values of the reference scene to classify the other two scenes was also investigated. The supervised classification looks very poor for the scene with the steepest incidence angle and quite reasonable for the other scene. The poor results of both the distance measure based automatic labelling and the pixel-wise classification of the scene with the steepest incidence angle may be related to incidence angle effects, e.g., brightness and resolution.

In Paper 3 (ch. 7), the classification potential of an initial subset of 44 features was investigated. We demonstrated that the classification performance of the selected method could be improved by systematically selecting the appropriate feature subset. Utilising all available features will degrade the classification result. A subset of only six features produced the best classification result. Comparison to a similar study led to the conclusion that the best feature subset is not unique for all quad-pol C-band scenes.

We believe that the proposed method will fit perfectly into a semi-automatic operational ice chart procedure. Experienced ice analysts can carefully select training data for each class present in the scene. Our method can then be utilised to choose the best feature subset. An automatic classification can then be produced from the selected subset. It is important to note that the proposed method is generic and can also be applied to single- and dual-pol SAR scenes and other frequencies.

The ideal classification is fully automatic. However, due to complications related to the features' seasonal variability and incidence angle dependence we do not currently consider fully automatic sea ice classification an option for operational use.

9.2 Remaining challenges

There are still challenges to overcome before automatic segmentations and/or classifications of SAR scenes can be used operationally. In this chapter we present some issues that we consider important for future research.

Efficient and robust automatic algorithms
In paper 1 we demonstrated the subjectivity of manually made ice chart. Several attempts and a lot of effort have been made trying to automate, and at the same time meet the strong requirements of efficiently producing robust ice charts. At present, we only know of one automatic system, the Map Guided Ice Classification (MAGIC) system [Leigh et al., 2014], considered for operational use. Thus, the words efficient, robust and automatic will still be highly relevant in the objectives for developing new, or improving existing sea ice classification algorithms.

Number of classes
The number of classes is a critical input parameter to the automatic algorithm we have utilised in Paper 1 and 2. Giving the algorithm too few classes will produce segments with class mixtures. A too large number of classes forces the algorithm to split homogeneous classes, just to attain the given number of classes. Estimating the number of classes input to an algorithm is a complicated problem. Future research should concentrate on automatic and robust estimation of the number of classes.

The World Meteorological Organization (WMO) SoD charts include one "class" termed "Ice of Undefined SoD" [MANICE, 2005]. This is a label the analysts use when it is not obvious which ice type a segment belongs to. A similar option should be incorporated in our classification algorithms. As discussed in Paper 2 and 3, our proposed method will always classify a group of pixels (segment) or a pixel to the statistically nearest reference ice class. This means that if a "new" ice class is present in a scene, it will not be recognized as a "new" ice class, but its pixels will be assigned to the ice type of the nearest reference class. To account for this shortage, the classification method could include a residue class. We consider it an important topic for future studies to implement such a residue class in automatic sea ice classification algorithms.

Extension to compact polarimetry
The spatial coverage of quad-pol SAR data is limited and hence not currently suitable for operational ice charting. Hence, investigating the extension of our method to the SAR systems with *compact polarimetry* (CP) modes will be important for future work.

The motivation for using CP is to maintain much of the polarimetric information available from quad-pol systems, while avoiding the quad-pol systems' disadvantages, e.g. reduced scene coverage, required power, limited choice in incidence [Raney, 2011].

Backscatter dependency of season, incidence angle and ice type
The presented methods exploit the discrimination power and interpretation of polarimetric parameters. Some of these are sensitive to incidence angle variations and seasonal changes. In particular, melting conditions result in considerable larger signature changes of the ice compared to freezing conditions [Gogineni and Moore, 1992, Kwok et al., 1992]. Thus, a thorough investigation of the parameters' incidence angle -, seasonal- and ice type dependency is considered to be important in order to improve the proposed method, especially with respect to operational applications.

Incidence angle correction
In Paper 2 three quad-pol scenes with different incidence angles were compared. A good incidence angle correction is crucial for comparing scenes obtained at different angles. The motivation for applying an incidence angle correction is to improve consistency of the backscatter magnitudes at various incidence angles. Incidence angle correction is a relevant topic for future studies. Such studies require carefully selected datasets, e.g., scenes acquired at the same environmental conditions, but with varying incidence angles. We have indications that an improved incidence angle correction could be performed by correcting each channel or each ice class independently.

Bibliography

[Arkett et al., 2008] M. Arkett, D. Flett and R. De Abreau. *C-band multiple polarization SAR for ice monitoring - what can it do for the Canadian Ice Service?*. In *Proc. Envisat Symp*. Montreux, Switzerland, 23-27 April 2008.

[Bertoia et al., 1998] C. Bertoia, J. C. Falkingham and F. Fetterer. *Polar SAR data for operational sea ice mapping*, chapter 10. Springer, 1998.

[Bertoia et al., 2004] C. Bertoia, M. Manore, H. S. Andersen, C. O'Connors, K. Q. Hansen and C. Evanego. *Synthetic aperture radar for operational ice observation and analusis at the U.S., Canadian, and Danish national ice centers*. In *Synthetic Aperture Radar Marine User's manual*, edited by C. Jackson and J. R. Apel, chapter 20, pp. 417 – 442. National Oceanic and Atmospheric Administration (NOAA), Washington, DC, September 2004.

[Canadian Centre for Remote Sensing, 2007] Canadian Centre for Remote Sensing. *Fundamentals of remote sensing*. http://www.nrcan.gc.ca/sites/ www.nrcan.gc.ca/files/earthsciences/pdf/resource/tutor/fundam/pdf/ fundamentals_e.pdf. Last visited in October 2014, 2007.

[Chen et al., 2014] S.-W. Chen, Y.-Z. Li, X. song Wang, S. ping Xiao and M. Sato. *Modeling and interpretation of scattering mechanisms in polarimetric synthetic aperture radar: Advances and perspectives*. IEEE Signal Processing Mag., **31**(4): 79–89, July 2014.

[Chuvieco and Huete, 2010] E. Chuvieco and A. Huete. *Fundamentals of Satellite Remote Sensing*. CRC Press, Boca Raton, FL, USA, 2010.

[Clausi and Deng, 2003] D. A. Clausi and H. Deng. *Operational segmentation and classification of SAR sea ice imagery*. In *Proc. IEEE Workshop Adv. Techn. Anal. Remotely Sensed Data*, pp. 268–275. Greenbelt, MD, USA, October 2003.

[Clausi et al., 2010] D. A. Clausi, A. K. Qin, M. S. Chowdhury, P. Yu and P. Maillard. *MAGIC: Map-guided ice classification system. Can. J. Remote Sens. Suppl.*, **36(1)**: S13 – S25, 2010.

[Cloude and Pottier, 1997] S. R. Cloude and E. Pottier. *An entropy based classification scheme for land applications of polarimetric SAR. IEEE Trans. Geosci. Remote Sens.*, **35**(1), 1997.

[Dierking and Busche, 2006] W. Dierking and T. Busche. *Sea ice monitoring by L-band SAR: An assessment based on literature and comparisons of JERS-1 and ERS-1 imagery. IEEE Trans. Geosci. Remote Sens.*, **44**(2): 957 – 970, April 2006.

[Dierking and Pedersen, 2012] W. Dierking and L. T. Pedersen. *Monitoring sea ice using Envisat ASAR - a new era starting 10 years ago.* In *Proc. IEEE IGARSS*, pp. 1852–1855. 2012.

[Dierking et al., 2004] W. Dierking, H. Skriver and P. Gudmandsen. *On the improvment of sea ice classification by means of radar polarimetry.* In *Proc. 23rd EARSel Symp. Remote Sens. Transition*, pp. 204 – 209. 2004.

[Doulgeris, 2013] A. P. Doulgeris. *A simple and extendable segmentation method for multi-polarisation SAR images.* In *Proc. POLinSAR 2013 – 6th Int. Workshop Sci. Applicat. SAR Polarimetry and Polarimetric Interferometry*, volume ESA SP-713, pp. 8. Frascati, Italy, 28 January - 1 February 2013.

[Drinkwater et al., 1992] M. R. Drinkwater, R. Kwok, E. Rignot, H. Israelsson, R. G. Onstott and D. P. Winebrenner. *Potential applications of polarimetry to the classification of sea ice.* In *Microwave remote sensing of sea ice*, edited by F. D. Carsey, number 68 in Geophysical Monograph, pp. 419–430. AGU, 1992.

[Eicken, 2013] H. Eicken. *Ocean science: Arctic sea ice needs better forecasts. Nature*, **497**: 431 – 433, May 2013.

[Eicken et al., 2009] H. Eicken, R. Gradinger, M. Salganek, K. Shirasawa, D. Perovish and M. Lepparanta, eds. *Field techniques for sea ice research.* University of Alaska Press, Fairbanks, 2009.

[Elachi and van Zyl, 2006] C. Elachi and J. van Zyl. *Introduction to the physics and techniques of remote sensing.* Wiley, Hoboken, New Jersey, USA, second edition, 2006.

[ESA Sentintel-1 Team, 2014] ESA Sentintel-1 Team. *Mission status report 29.* https://sentinel.esa.int/documents/247904/1484135/Sentinel-1-Mission_Status_Report_29-Period_21-27_October_2014. last visited in october 2014, European Space Agency, 2014. Reference period: 21 - 27 October.

[Falkingham, 2014] J. C. Falkingham. *Global satellite observation requirements for floating ice: Focusing on synthetic aperture radar.* http://nsidc.org/noaa/iicwg/docs/IICWG-2014/Global-Satellite-Observation-Requirements-for-Floating-Ice-Final.pdf. last visited in october 2014., Contract report for Environment Canada, March 2014.

[Freeman and Durden, 1998] A. Freeman and S. L. Durden. *A three-component scattering model for polarimetric SAR data. IEEE Trans. Geosci. Remote Sens.*, **36**(3): 964 – 973, May 1998.

[Gill and Yackel, 2012] J. Gill and J. Yackel. *Evaluation of C-band SAR polarimetric parameters for discriminating of first-year sea ice types. Can. J. Remote Sens.*, **38**(3): 306–323, 2012.

[Gill et al., 2010] J. Gill, M. Fueller and J. J. Yackel. *Examination of C-band polarimetric SAR backscatter response of snow covered first-year sea ice*. In *The Prairie Summit*. Regina, Saskwtchewen, Canada, June 1 - 7 2010.

[Gogineni and Moore, 1992] S. P. Gogineni and R. K. Moore. *The effects of freeze-up and melt processes on microwave signatures*. In *Microwave remote sensing of sea ice*, edited by F. D. Carsey, number 68 in Geophysical Monograph, chapter 17, pp. 329 – 354. AGU, 1992.

[Griffiths and College, 1999] D. J. Griffiths and R. College. *Introduction to electrodynamics*. Prentice Hall, Upper Saddle River, New Jersey, USA, third edition, 1999.

[Haas et al., 2009] C. Haas, J. Lobach, S. Hendricks, L. Rabenstein and A. Pfaffling. *Helicopterborne measurements of sea ice thickness, using a small and lightweight, digital EM system. J. Appl. Geophys.*, **67(3)**: 234–241, 2009.

[Hajnsek et al., 2003] I. Hajnsek, E. Pottier and S. Cloude. *Inversion of surface parameters from polarimetric SAR. IEEE Trans. Geosci. Remote Sens*, **41**(4): 727–744, April 2003.

[Hallikainen and Winebrenner, 1992] M. Hallikainen and D. Winebrenner. *The physical basis for sea ice remote sensing*. In *Microwave remote sensing of sea ice*, edited by F. D. Carsey, number 68 in Geophysical Monogr., chapter 3, pp. 73–104. AGU, 1992.

[Hossain, 2012] M. Hossain. *Polarimetric Synthetic Aperture Radar Measurements of Snow Covered First-Year Sea Ice*. Ph.D. thesis, Department of Geography, University of Calgary, Canada, September 2012.

[Ice Observation Handbook, 1984] Ice Observation Handbook. *Prepared by: Commanding officer*. Technical report, Naval Polar Oceanography Center, 4301 Suitland Rd, Washington DC 20390, 1984.

[IEEE standards, 2003] IEEE standards. *IEEE standard letter designations for radar-frequency bands*. IEEE Std 521-2002 (Revision of IEEE Std 521-1984), 2003. 10.1109/IEEESTD.2003.94224.

[Jiao et al., 2011] X. Jiao, H. McNairn, J. Shang, E. Pattey, J. Liu and C. Champagne. *The sensitivity of RADARSAT-2 polarimetric SAR data to corn and soybean leaf area index. Can. J. Remote Sens.*, **37**(1): 69–81, 2011.

[Kwok et al., 1992] R. Kwok, G. Cunningham and B. Holt. *An approach to identifation of sea ice types from spaceborne SAR data*. In *Microwave remote sensing of sea ice*, edited by F. D. Carsey, number 68 in Geophysical Monograph, chapter 19, pp. 355 – 360. AGU, 1992.

[Kwok et al., 1998] R. Kwok, S. Nghiem, S. Martin, D. Winebrenner, A. Gow, D. Perovich, C. Swift, D. Barber, K. Golden and E. Knapp. *Laboratory measurements of sea ice: connections to microwave remote sensing*. IEEE Trans. Geosci. Remote Sens., **36**(5): 1716–1730, September 1998.

[Kwok et al., 2009] R. Kwok, G. F. Cunningham, M. Wensnahan, I. Rigor, H. J. Zwally and D. Yi. *Thinning and volume loss of the arctic ocean sea ice cover: 2003 - 2008. J. Geophys. Res*, **114**: C07005, 2009.

[Kwon et al., 2013] T.-J. Kwon, J. Li and A. Wong. *ETVOS: an enhanced total variation optimization segmentation approach for sar sea-ice image segmentation. IEEE Trans. Geosci. Remote Sens.*, **51(2)**: 925 – 934, 2013.

[Lee and Pottier, 2009] J.-S. Lee and E. Pottier. *Polarimetric Radar Imaging, from basics to applications*. CRC Press, Boca Raton, FL, USA, February 2009.

[Lee et al., 1999] J.-S. Lee, M. Grunes, T. Ainsworth, L.-J. Du, D. Schuler and S. Cloude. *Unsupervised classification using polarimetric decomposition and the complex wishart classifier. Geoscience and Remote Sensing, IEEE Transactions on*, **37**(5): 2249–2258, Sep 1999.

[Lee, 2012] P. M. Lee. *Bayesian Statistics: An Introduction*. John Wiley, fourth edition, June 2012.

[Leigh et al., 2014] S. Leigh, Z. Wang and D. Clausi. *Automated ice-water classification using dual polarization SAR satellite imagery. IEEE Trans. Geosci. Remote Sens.*, **52**(9): 5529–5539, Sept 2014.

[MANICE, 2005] MANICE. *Manual of Standard Procedures for Observing and Reporting Ice Conditions*. Canadian Ice Service, Ottawa, Ontario, Canada, 2005. ISBN: 0-660-62858-9.

[Maslanik et al., 2011] J. Maslanik, J. Stroeve, C. Fowler and W. Emery. *Distribution and trends in arctic sea ice age through spring 2011. Geophys. Res. Lett.*, **38(11)**: L13502, 2011.

[Massom and Lubin, 2006a] R. Massom and D. Lubin. *Polar Remote Sensing - Atmosphere and Oceans*, volume I. Praxis Publishing Ltd., 2006a.

[Massom and Lubin, 2006b] R. Massom and D. Lubin. *Polar Remote Sensing - Ice Sheets*, volume II. Praxis Publishing Ltd., 2006b.

[McCandless Jr. and Jackson, 2004] S. W. McCandless Jr. and C. R. Jackson. *Principles of synthetic aperture radar*. In *Synthetic Aperture Radar Marine User's manual*, edited by C. Jackson and J. R. Apel, chapter 1, pp. 1 – 23. National Oceanic and Atmospheric Administration (NOAA), Washington, DC, September 2004.

[Moen et al., 2013a] M.-A. Moen, A. Doulgeris, S. Anfinsen, A. Renner, N. Hughes, S. Gerland and T. Eltoft. *Comparison of feature based segmentation of full polarimetric SAR satellite sea ice images with manually drawn ice charts*. The Cryosphere, **7**: 1693 − 1705, 2013a.

[Moen et al., 2013b] M.-A. Moen, L. Ferro-Famil, A. P. Doulgeris, S. Anfinsen, S. Gerland and T. Eltoft. *Polarimetric decomposition analysis of sea ice data*. In *Proc. POLinSAR 2013*, p. 7pp. Frascati, Italy, 28 January - 1 February 2013b.

[Morena et al., 2004] L. C. Morena, K. V. James and J. Beck. *An introduction to the radarsat-2 mission*. Can. J. Remote Sens., **30**(3): 221 − 234, 2004.

[National Ice Center, 2006] National Ice Center. *National ice center arctic sea ice charts and climatologies in gridded format*. http://dx.doi.org/10.7265/N5X34VDB, Boulder, Colorado, USA, 2006.

[Nghiem and Bertoia, 2001] S. V. Nghiem and C. Bertoia. *Study of multi-polarization C-band backscatter signatures for Arctic sea ice mapping with future satellite SAR*. Can. J. Remote Sens., **27**(5): 387− 402, 2001.

[Nicholson, 1995] W. K. Nicholson. *Linear Algebra with applications*. PWS Publishing Company, Boston, MA, USA, third edition, 1995.

[Oliver and Quegan, 2004] C. Oliver and S. Quegan. *Understanding Syntheric Aperture Radar Images*. SciTech Publishing Inc., Rayleigh, USA, 2004.

[Onstott, 1992] R. Onstott. *SAR and scatterometer signatures of sea ice*. In *Microwave remote sensing of sea ice*, edited by F. D. Carsey, number 68 in Geophysical Monograph, pp. 73 −104. AGU, 1992.

[Onstott and Shuchman, 2004] R. G. Onstott and R. A. Shuchman. *Sar measurements of sea ice*. In *Synthetic Aperture Radar Marine User's manual*, edited by C. Jackson and J. R. Apel, chapter 3, pp. 81 − 115. National Oceanic and Atmospheric Administration (NOAA), Washington, DC, September 2004.

[Parmeter and Coon, 1972] R. R. Parmeter and M. D. Coon. *Model of pressure rige formation in sea ice*. J. Geophys. Res, **77**(33): 6565 − 6575, November 1972.

[Partington et al., 2010] K. C. Partington, J. D. Fletch, D. A. Barber, D. Isleifson, P. J. Meadows and P. Verlaan. *Dual-polarization C-band radar observations of sea ice in the Amundsen Gulf*. IEEE Trans. Geosci. Remote Sens., **48**(6): 2685 −2691, June 2010.

[Raney, 2011] R. Raney. *A persepctive on copact polarimetry*. IEEE Geosci. Remote Sens. Newslett., pp. 12 − 18, September 2011.

[Renner et al., 2013] A. H. H. Renner, S. Hendricks, S. Gerland, J. Beckers, C. Haas and T. Krumpen. *Large-scale ice thickness distribution of first-year sea ice in spring and summer north of svalbard. Ann. of Glaciol.*, **54**(62): 13–18, 2013.

[Sandven and Johannessen, 2006] S. Sandven and O. M. Johannessen. *Sea ice monitoring by Remote Sensing*, volume 6, manual of remote sensing 8, pp. 241 – 283. American Society for Photogrammetry and Remote Sensing, Maryland, USA, third edition, 2006.

[Scheuchl et al., 2001] B. Scheuchl, R. Caves, I. Cumming and G. Staples. *Automated sea ice classification using spaceborne polarimetric SAR data.* In *Proc. IGARSS 2001*, pp. 3117–3119. 2001.

[Scheuchl et al., 2004a] B. Scheuchl, R. Caves, D. Flett, R. De Abreau, M. Arkett and I. G. Cumming. *The potential of cross-polarization information for operational sea ice monitoring*. In *Proc. ENVISAT/ERS Symp.* Salzburg, Austria, September 6 - 10 2004a.

[Scheuchl et al., 2004b] B. Scheuchl, D. Flett, R. Caves and I. Cumming. *Potential of RADARSAT-2 data for operational sea ice monitoring. Can. J. Remote Sens.*, **30**(3): 448–461, 2004b.

[Schuler and Lee, 2006] D. L. Schuler and J.-S. Lee. *Mapping ocean surface features using biogenic slick-fields and SAR polarimetric decomposition techniques. IEE Proc. Radar, Sonar Navig.*, **153**: 260 – 270, June 2006.

[Sephton and Partington, 1998] A. J. Sephton and K. C. Partington. *Towards Operational Monitoring of Arctic Sea Ice by SAR*, chapter 12. Springer, 1998.

[Smith, 2007] O. P. Smith. *Observers guide to sea ice*. Technical report, National Oceanic and Atmospheric Administration (NOAA) Ocean Service, August 2007.

[Stocker et al., 2013] T. Stocker, D. Qin, G.-K. Plattner, M. Tignor, S. Allen, J. Boschung, A. Nauels, Y. Xia, V. Bex and P. M. (eds.). *Climate Change 2013: The Physical Science Basis. Working Group I Contribution to the Fifth Assessment Report of the Intergovernmental Panel on Climage Change.* Technical report, Cambridge University Press, Cambridge, United Kingdom and New York, NY, USA, 2013.

[Thomsen et al., 1998a] B. Thomsen, S. Nghiem and R. Kwok. *Polarimetric C-band SAR observations of sea ice in the Greenland Sea.* In *Proc. IGARSS 1998*, pp. 2502–2504. 1998a.

[Thomsen et al., 1998b] B. Thomsen, L. Pedersen, H. Skriver and W. Dierking. *Polarimetric EMISAR observations of sea ice in the Greenland Sea.* In *Future Trends in Remote Sensing*, edited by P. Gudmandsen, pp. 345–351. Taylor & Francis, 1998b.

[Torres et al., 2012] R. Torres, P. Snoeij, D. Geudtner, D. Bibby, M. Davidson, E. Attema, P. Potin, B. Rommen, N. Floury, M. Brown, I. N. Traver, P. Deghaye, B. Duesmann, B. Rosich, N. Miranda, C. Bruno, M. L'Abbate, R. Croci, A. Pietropaolo, M. Huchler and F. Rostan. *GMES sentinel-1 mission*. *Remote Sensing of Environment*, **120**(0): 9 – 24, 2012. The Sentinel Missions - New Opportunities for Science.

[Touzi, 2004] R. Touzi. *Target scattering decomposition of one-look and multi-look SAR data using a new coherent scattering model: the TSVM*. In *Geoscience and Remote Sensing Symposium, 2004. IGARSS '04. Proceedings. 2004 IEEE International*, volume 4, pp. 2491–2494 vol.4. Sept 2004.

[Touzi, 2007] R. Touzi. *Target scattering decomposition in terms of roll-invariant target parameters. IEEE Trans. Geosci. Remote Sens.*, **45**(1): 73–84, Jan 2007.

[Tucker III et al., 1992] W. Tucker III, D. Perovich and A. Gow. *Physical properties of sea ice relevant to remote sensing*. In *Microwave remote sensing of sea ice*, edited by F. D. Carsey, number 68 in Geophysical Monogr., chapter 2, pp. 73–104. AGU, 1992.

[Wackerman, 1992] C. Wackerman. *Digital SAR image formation*. In *Microwave remote sensing of sea ice*, edited by F. D. Carsey, number 68 in Geophysical Monogr., chapter 6, pp. 73–104. AGU, 1992.

[Winkler, 2006] G. Winkler. *Image Analysis, Random Fields and Markov Chain Monte Carlo Methods*. Springer, Heidelberg, Germany, second edition, 2006.

[WMO-No.574, 2010] WMO-No.574. *Sea-ice information services in the world*. Technical Report 574, World Meteorological Organization, 2010.

[Woodhouse, 2006] I. H. Woodhouse. *Introduction to Microwave Remote Sensing*. Taylor & Francis, 2006.

[World Meteorological Organization, 2004] World Meteorological Organization. *Ice chart colour code standard*. Technical Report WMO/TD-No.1215, JCOMM Technical Report No.24, Geneva, Switzerland, 2004.

[Yamaguchi et al., 2005] Y. Yamaguchi, T. Moriyama, M. Ishido and H. Yamada. *Four-component scattering model for polarimetric SAR image decomposition. IEEE Trans. Geosci. Remote Sens.*, **43**(8): 1699–1706, Aug 2005.

[Zakhvatkina et al., 2013] N. Zakhvatkina, V. Alexandrov, O. Johannessen, S. Sandven and I. Frolov. *Classification of sea ice types in ENVISAT synthetic aperture radar images.. IEEE Trans. Geosci. Remote Sens.*, **51(5)**: 2587 – 2600, 2013.

[van Zyl and Kim, 2011] J. van Zyl and Y. Kim. *Synthetic Aperture Radar Polarimetry*. Wiley, Hoboken, New Jersey, USA, 2011.

[van Zyl et al., 2008] J. van Zyl, Y. Kim and M. Arii. *Requirements for model-based polarimetric decompositions.* In *IEEE Int. Geosci. Remote Sens. Symp. (IGARSS)*, volume 5, pp. V − 417–V − 420. July 2008.

[van Zyl et al., 2011] J. van Zyl, M. Arii and K. Yunjin. *Model-based decomposition of polarimetric SAR covariance matrices constrained for nonnegative eigenvalues. IEEE Trans. Geosci. Remote Sens.*, **49**(9): 3452–3459, Sept 2011.